THE JOURNAL OF PHYSICAL CHEMISTRY B
A JOURNAL OF THE AMERICAN CHEMICAL SOCIETY

pubs.acs.org/JPCB

Article

Investigating How Lysophosphatidylcholine and Lysophosphatidylethanolamine Enhance the Membrane Permeabilization Efficacy of Host Defense Peptide Piscidin 1

Published as part of The Journal of Physical Chemistry B special issue "The Dynamic Structure of the Lipid Bilayer and Its Modulation by Small Molecules".

Amy Rice,[△] Andriana C. Zourou,[△] Evan P. Goodell, Riqiang Fu, Richard W. Pastor,* and Myriam L. Cotten*

Cite This: *J. Phys. Chem. B* 2025, 129, 210−227

Read Online

ACCESS | Metrics & More | Article Recommendations | Supporting Information

ABSTRACT: Lysophospholipids (LPLs) and host defense peptides (HDPs) are naturally occurring membrane-active agents that disrupt key membrane properties, including the hydrocarbon thickness, intrinsic curvature, and molecular packing. Although the membrane activity of these agents has been widely examined separately, their combined effects are largely unexplored. Here, we use experimental and computational tools to investigate how lysophosphatidylcholine (LPC) and lysophosphatidylethanolamine (LPE), an LPL of lower positive spontaneous curvature, influence the membrane activity of piscidin 1 (P1), an α-helical HDP from fish. Four membrane systems are probed: 75:25 C16:0-C18:1 PC (POPC)/C16:0-C18:1 phosphoglycerol (POPG), 50:25:25 POPC/POPG/16:0 LPC, 75:25 C16:0-C18:1 PE (POPE)/POPG, and 50:25:25 POPE/POPG/14:0 LPE. Dye leakage, circular dichroism, and NMR experiments demonstrate that while the presence of LPLs alone does not induce leakage-proficient defects, it boosts the permeabilization capability of P1, resulting in an efficacy order of POPC/POPG/16:0 LPC > POPE/POPG/14:0 LPE > POPC/POPG > POPE/POPG. This enhancement occurs without altering the membrane affinity and conformation of P1. Molecular dynamics simulations feature two types of asymmetric membranes to represent the imbalanced ("area stressed") and balanced ("area relaxed") distribution of lipids and peptides in the two leaflets. The simulations capture the membrane thinning effects of P1, LPC, and LPE, and the positive curvature strain imposed by both LPLs is reflected in the lateral pressure profiles. They also reveal a higher number of membrane defects for the P1/LPC than P1/LPE combination, congruent with the permeabilization experiments. Altogether, these results show that P1 and LPLs disrupt membranes in a concerted fashion, with LPC, the more disruptive LPL, boosting the permeabilization of P1 more than LPE. This mechanistic knowledge is relevant to understanding biological processes where multiple membrane-active agents such as HDPs and LPLs are involved.

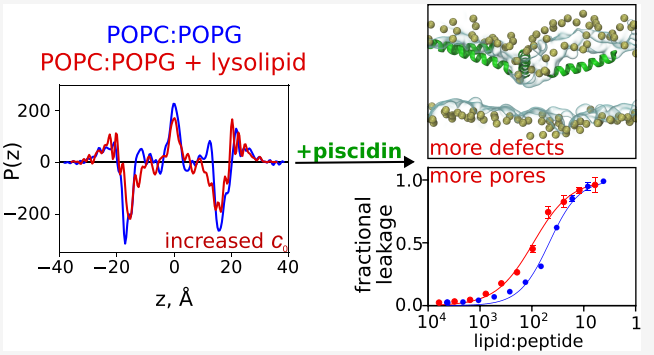

INTRODUCTION

The unique structures, dynamics, and functions of biological membranes are potentiated by a broad range of phospholipids.[1−7] Among them, lysophospholipids (LPLs) have attracted attention due to their unique biochemical and biophysical properties.[8−14] LPLs are produced through membrane metabolism when phospholipases cleave the sn-1 or sn-2 acyl chains ("tail") of bilayer phospholipids such as phosphatidylcholine (PC).[15] Lacking one tail, LPLs exhibit nonbilayer forming properties and favor micellar phases.[16,17] Depending on their membrane-partitioning properties and concentration, their membrane-disruptive effects can range from altering the spontaneous curvature and thickness to inducing lysis through detergent-like effects.[9,11,18] Interestingly, similar effects are also associated with membrane-active peptides (MAPs), a large family of bioactive peptides that can interact with LPL-containing membranes as part of their biological activities.[11,14,19,20]

While the membrane-disruptive effects of LPLs and MAPs have been widely examined separately, their combined action

Received: August 29, 2024
Revised: November 12, 2024
Accepted: November 20, 2024
Published: December 16, 2024

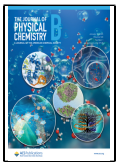

https://doi.org/10.1021/acs.jpcb.4c05845
J. Phys. Chem. B 2025, 129, 210−227

remains largely unexplored.[8−14,21−26] In particular, analyses are lacking to quantify their cumulative effects on the stability and permeability of membranes. This knowledge gap limits our ability to mechanistically describe biological functions that involve these two classes of membrane-active agents. For instance, it remains unclear how the LPLs present in pathogenic membranes or used as bactericidal agents influence the permeabilization effects of membrane-interacting host defense peptides (HDPs), a category of MAPs that eradicate bacteria through membrane activity.[21,22,24,25,27−34] Overcoming this lack of mechanistic understanding is important since HDPs have garnered significant interest in the search for novel therapeutics to fight antibiotic-resistant bacteria.[29,30,35−43]

In this research, we investigate the interactions of LPL-containing membranes with piscidin 1 (P1, FFHHIFRGIVHVGKTIHRLVTG)), a fish HDP.[44,45] As archetype α-helical, amphipathic, and membrane-disruptive HDPs, piscidins exhibit antimicrobial potency that is commensurate with their membrane activity.[46−54] They are active on a broad range of Gram-positive and Gram-negative bacteria, including *Helicobacter pylori* (*H. pylori*).[55] A Gram-negative bacterium implicated in gastric adenocarcinomas and peptic ulcers, *H. pylori*, exhibits increased levels of lysophosphatidylethanolamine (LPE) when it becomes virulent.[56,57] More specifically, the LPE content, which is only 2% in the *Hp*L variant that does not attach to epithelial cells, grows to 33% in the *Hp*S variant that produces the VacA toxin and invades epithelial cells.[56] This dramatic upregulation of LPE in the bacterial membranes, where piscidin performs its antimicrobial activity, represents an excellent example of biological systems where multiple membrane-active agents are present when function is performed.

Mechanistically, LPLs and HDPs exert membrane activity by disrupting the molecular packing of the lipid molecules present in the membrane, resulting in altered intermolecular interactions across the bilayer and a redistribution of the lateral pressures.[11,16,17,58−60] These are positive (repulsive) in the headgroup and acyl chain regions, negative (attractive/cohesive) at the polar−apolar interfacial region, and positive in the bilayer midplane. Models have predicted that the addition of nonbilayer forming LPLs such as LPE and lysophosphatidylcholine (LPC) changes the lateral pressure profile, resulting in the buildup of positive spontaneous curvature.[16,61,62]

The stored curvature stress induced by LPLs represents a source of energy that can be used to drive biological processes and functions, such as the conformational changes of ion channels (e.g., gramicidin A),[63] the bilayer association of peripheral membrane proteins (e.g., phospholipase A2),[64] and the activation of mechanosensitive channels (e.g., MscL and MscS from *Escherichia coli* (*E. coli*))[50] This energy is sufficient to enable events that would otherwise be inhibited, such as the permeabilization of membranes by fusion peptides and the tilting of MAPs into membranes.[19,62,65] With regard to the latter, Ulrich and co-workers[19,65] specifically demonstrated that the positive curvature strain imposed by LPC enables synthetic α-helical MAPs to transition from a surface-bound to transmembrane orientation.

We previously showed that similarly to LPLs, P1 and its isoform P3 also produce positive spontaneous curvature.[66] This effect was observed by molecular dynamics (MD) simulation in 75:25 1-palmitoyl-2-oleoyl-*sn*-glycero-3-phosphocholine (POPC)/1-palmitoyl-2-oleoyl-*sn*-glycero-3-phosphoglycerol (POPG), 1:1 1-palmitoyl-2-oleoyl-*sn*-glycero-3-phosphoethanolamine (POPE)/POPG, and 80:20 POPC/Cholesterol (Chol). In these lipid mixtures, the PO-acyl chains experience the "basket effect" and significant thinning as they wrap around the interfacially bound peptides to fill the gaps between the peptides and bilayer midplane.[66] MD simulations support the notion that the peptides induce permeabilization by forming funnel-like defects in these thinned membranes.[50,51,67−69]

Due to their induction of positive curvature, P1 and P3 significantly disrupt membranes that contain PE, a lipid associated with negative spontaneous curvature generation. In model membranes, the peptides prevent PE from forming its preferred state, the hexagonal HII phase.[50] Since the peptides preferentially concentrate at the PE-rich septal regions of bacteria, their curvature-inhibitory effect on PE could help explain how they disrupt cell division. Their alteration of curvature in PE-containing membranes also correlates with their ability to lower the activation threshold of the mechanosensitive channels that exist in the PE-rich inner membrane of *E. coli*.[50]

Given that both P1 and LPLs exert positive curvature strain on membranes, we hypothesized that P1 would experience enhanced disruptive and permeabilization effects on membranes containing LPLs such as LPC and LPE, and that the magnitude of these effects would reflect that LPC induces stronger positive curvature strain than LPE.[8] We predicted that the increased membrane permeabilization efficacy of P1 would be associated with altered membrane properties such as reduced hydrocarbon thickness, and increased curvature strain and propensity for defect formation. We used biophysical experiments and MD simulations to make the measurements needed to test this hypothesis.

We added 16:0 LPC to the host model membrane 75:25 C16:0-C18:1 PC (POPC)/C16:0-C18:1 PG (POPG) to form 50:25:25 POPC/POPG/16:0 LPC, and 14:0 LPE to modify 75:25 POPC/POPG to 50:25:25 POPE/POPG/14:0 LPE. Several considerations informed our selection of membrane systems. First, we selected 16:0 LPC since it is one of the most common LPLs in biological membranes.[70] Furthermore, it has already been the subject of numerous studies that have characterized its impact on membranes, including its strong ability to induce positive curvature strain.[8,19,62,65,71] Second, we chose 75:25 POPC/POPG as the host membrane for LPC because the headgroup of the zwitterionic lipid is also PC and this model system has been widely used to mimic bacterial cell membranes.[48,49,51,72−78] Third, to capture that bacterial membranes contain PE as the zwitterionic lipids, we used 75:25 POPE/POPG as another host membrane system and LPE as the LPL. We used C14:0 as the acyl chain knowing that the plasma membrane of *H. pylori* is abundant in this fatty acid.[56] Fourth, we incorporated 25% LPL in each host membrane since this would be in the range needed to influence the membrane curvature and HDP behavior.[1,8−10,19,65] Furthermore, it is also in line with the high content of LPE observed in *H. pylori*.[56] Notably, LPC adds more curvature strain to bilayers than LPE,[8] providing us with a way to test the effects of LPLs with varying curvature-inducing properties. As elaborated in the Discussion, while all of the components of a lipid contribute to its spontaneous curvature generation, both experiments and simulations indicate that the headgroup is the dominant factor. Hence, the difference in chain lengths of the 16:0 LPC and 14:0 LPE studied here should not be a confounding factor.

https://doi.org/10.1021/acs.jpcb.4c05845
J. Phys. Chem. B 2025, 129, 210−227

Dye leakage assays were performed to quantify membrane activity of P1 and P1−Cu^{2+} on the LPC- and LPE-containing membranes. We included the metalated state of P1 given that it is more membrane-active and antimicrobial than the apo state.[73,79,80] Metalation occurs through the amino-terminal copper and nickel (ATCUN) motif of the peptide.[73,80−83] Enhanced membrane disruption upon metalation has been explained by the deeper membrane insertion of the N-terminal region.[81,82] The secondary structure of P1 and binding affinity to LPL-containing membranes was followed by circular dichroism (CD). Using ^{15}N-labeled peptides, we employed solid-state NMR to characterize the orientation of the peptide in the LPL-containing membranes. The structural arrangement of the lipids in the presence of P1 was studied using ^{31}P NMR.

In parallel to the experimental work, MD simulations were carried out to quantify membrane thickness, spontaneous curvature, and the number of defects; to characterize the membrane conformation of the peptides; and to explore the defects hypothesized to be the early steps of permeabilization. The MD simulations were carried out using two distinct initial conditions that represent a novel approach. For the first, ten P1 were inserted into one leaflet (defined cis) of bilayers that were symmetric in both composition and lipid number. These are denoted "area stressed" (AS) as the membrane experiences considerable differential surface tension (or stress) due to the large area mismatch. These conditions model a bilayer in which lipids are not able to translocate (flip-flop) to the opposing leaflet to relieve the area stress induced by piscidin binding. The second initial condition was equilibrated using $P2_1$ boundary conditions,[84,85] which allows lipids to switch leaflets, equalizing their chemical potential on each side of the bilayer; these bilayers are denoted "area relaxed" (AR). This setup, which corresponds to the more commonly used method for building asymmetric bilayers, models a membrane that can rearrange to accommodate the inserted peptides. Hence, our two initial conditions represent the two extremes that could be encountered experimentally: maximal differential stress versus relaxed stress and equalized chemical potential between leaflets.

Following the Results section, we discuss how our joined experimental and computational studies deepen our mechanistic understanding of biological processes that involve multiple membrane-active agents such as LPLs and HDPs. Comments on predicting the effects of lipids on membrane spontaneous curvature by their idealized shape (an inverted cone for lysophospholipids) are included.

METHODS

Materials. Unless otherwise indicated, all chemicals were purchased from Fisher Scientific (Hampton, NH). The lipids involved in this research were obtained from Avanti Polar Lipids (Alabaster, AL) and included 1-palmitoyl-2-oleoyl-*sn*-glycero-3-phosphocholine (POPC), 1-palmitoyl-2-oleoyl-*sn*-glycero-3-phosphoethanolamine (POPE), 1-palmitoyl-2-oleoyl-*sn*-glycero-3-phospho-(1′-*rac*-glycerol) (POPG), 1,2-dimyristoyl-*sn*-glycero-3-phosphocholine (DMPC), 1-myristoyl-2-hydroxy-*sn*-glycero-3-phosphocholine (14:0 LPC), 1-palmitoyl-2-hydroxy-*sn*-glycero-3-phosphocholine (16:0 LPC), and 1-myristoyl-2-hydroxy-*sn*-glycero-3-phosphoethanolamine (14:0 LPE). Isotopically labeled amino acids were acquired from Cambridge Isotope Laboratories (Tewksbury, MA) and Millipore Sigma (Burlington, MA).

Peptides. Peptides were made by solid-phase synthesis at the Tufts University Core Facility (Boston, MA) and the University of Texas Southwestern Medical Center (Dallas, TX), as previously described.[74] For peptides investigated by ^{15}N NMR, isotopically labeled amino acids were incorporated at selected amide nitrogen sites. Purification was carried out by reverse phase HPLC using a gradient of water/acetonitrile with 0.1% TFA, as previously outlined.[51] To remove the trifluoroacetate ions and produce the hydrochloride salt form of the peptides, the peptides were dissolved in dilute HCl. Following lyophilization, the excess salt was removed by dialysis using bags with 1.0 kDa molecular weight cutoff (MWCO) (Repligen, Waltham, MA). The peptides were then reconstituted in water prior to amino acid analysis (AAA) at the Protein Chemistry Lab at Texas A&M University (College Station, TX) to yield the concentrations of the solutions and verify the amino acid content of the peptides. Metalation of the peptides was achieved using stoichiometric amounts of $CuCl_2$, as previously explained.[73,83] For NMR, metalation was done with $NiCl_2$ to produce a diamagnetic complex (Cu^{2+} binding to the ACTUN motif would yield a paramagnetic complex).[83,86] The pH was adjusted with HCl and NaOH to 7.4 after adding the metal ion.

Calcein Release from Lysophospholipid-Containing Vesicles. The permeabilization effects of the peptides were measured using the calcein leakage assay as previously reported.[73] To make large unilamellar vesicles (LUVs), 4 μmol of lipids was dissolved in chloroform. The solvent was removed using a stream of nitrogen gas prior to lyophilization overnight. The lipid film was then hydrated with 300 μL of 80 mM calcein dye (Millipore Sigma, Burlington, MA) and 4 freeze−thaw cycles were performed prior to extrusion through a mini extruder (Avanti Polar Lipids, Alabaster, AL) fitted with a 0.1 μm polycarbonate membrane filter (Whatman, Florham Park, NJ). To remove the free dye, the resulting LUVs were run through a size exclusion Sephadex G-50 column (GE Healthcare, Pittsburgh, PA) with degassed 4-(2-hydroxyethyl)-1-piperazineethanesulfonic acid (HEPES) buffer (50 mM, 100 mM NaCl, 3 mM EDTA, 0.01% w/v NaN_3, pH 7.4) as the mobile phase. This step requires that the vesicles be in the fluid state. All vesicles, including those containing 14:0 LPE were successfully purified, confirming their fluid state. A phosphorus assay was conducted to determine the precise lipid concentration.[87,88] The LUVs were typically diluted 25-fold with the buffer before platting 180 μL per well in a 96-well plate (Fisher Scientific, Hampton, NH). Then, 20 μL of peptide solution from serially diluted stocks in water were added to each well to reach peptide-to-lipid ratios (P/L) equal to 1:512, 1:256, 1:128, 1:64, 1:32, 1;16, 1:8, and 1:4. With the metalated peptides, additional dilutions were prepared to cover lower P/L ratios and obtain full leakage curves. After 60 min of incubation with shaking conditions of 142 rpm, fluorescence was measured on a BioTek H4 Synergy Hybrid Microplate Reader (Agilent, Santa Clara, CA) with excitation at 490 nm and emission at 520 nm. The stability of the vesicles was verified by checking that the fluorescence of the samples not treated with peptide was stable over time. Increased fluorescence in peptide-containing wells corresponded to the release of the trapped calcein. The fractional leakage was calculated using eq 1:

https://doi.org/10.1021/acs.jpcb.4c05845
J. Phys. Chem. B 2025, 129, 210−227

$$\text{fractional calcein leakage} = \frac{I_x - I_{\text{background}}}{I_{\text{Triton}} - I_{\text{background}}} \quad (1)$$

where I_x is the fluorescence intensity after the incubation at each temperature, $I_{\text{background}}$ corresponds to the negative control (180 μL of LUVs with 20 μL of water), and I_{Triton} is the positive control producing 100% leakage (180 μL of LUVs with 20 μL of 0.1% v/v Triton X-100 detergent).

The normalized data were fitted in GraphPad Prism (GraphPad, San Diego, CA) using eq 2:

$$Y = 1 - \frac{1}{1 + \left(\left(\frac{x}{EC_{50}}\right)^p\right)} \quad (2)$$

where p is a cooperativity coefficient and EC_{50} is the half-maximal effective peptide-to-lipid ratio (P/L) concentration for each of the peptides.[89] Statistical analysis was done in Microsoft Excel. A two-tailed t test with unequal variance was performed to compare the different EC_{50} values.

Circular Dichroism-Monitored Titrations. CD was used to characterize the binding affinity of the peptides for membranes as recently reported.[48] Each lipid film contained 11 μmol of lipids. The appropriate amount of lipid stocks was added to a round-bottom flask and the organic solvent evaporated using a stream of N_2 gas. The films were lyophilized overnight to remove any residual solvent. Hydration of the films with buffer (3 mM potassium phosphate, pH 7.4) was followed by 4 freeze thaw cycles to homogenize the mixture. To create LUVs, extrusion was performed through a 0.2 μm membrane (Whatman, Maidstone, UK) in an Avanti Polar Lipid Mini Extruder (Alabaster, AL). Titrations were done by mixing each peptide with increasing amounts of LUVs, so that P/L ranged from 1:2 to 1:120. The peptide concentration was kept constant at 20 μM. Spectra were acquired on a Jasco 1500 instrument (Easton, MD) from 260 to 190 nm using a resolution of 0.1 nm, sensitivity of 100 millidegrees, bandwidth of 1.0 nm, response of 8 s, and scan speed of 20 nm/min over 3 accumulations. Data collected in the presence of the peptide were corrected for the contribution from the LUVs by subtracting the signal obtained from a blank containing the LUVs but no peptide.

The percent α-helical content adopted by the peptide at each P/L ratio was obtained using the mean residue ellipticity of the peptide at 222 nm, as previously described.[90] The mean residue ellipticity for 100% α-helical content was assumed to be −39,500 deg × cm^2/dmol.[91−93] A Langmuir model was used to fit the binding isotherm and yield the dissociation constant, K_D.[94] Two replicates were run and GraphPad Prism (GraphPad, San Diego, CA) was used to analyze the data through least-squares fitting and produce an error bar.

Preparation of Samples for Oriented Solid-State NMR. Oriented solid-state NMR samples were prepared using a previously established protocol.[48,74] Briefly, after combining the lipids in a round-bottom flask, the organic solvent was evaporated using a stream of N_2 gas. The samples were then lyophilized overnight before being hydrated with 8.0 mL of BisTris buffer (3 mM, pH 7.4). The peptide (~2.5 mg), dissolved in 2 mL of water, was added to the lipid at P/L = 1:60. Metalation was performed, as previously explained, with the pH adjusted to 7.4.[73] The peptide-lipid suspension was incubated overnight at 40 °C. Ultracentrifugation was then performed for 1 h 40 min using a Beckman Optima-90K centrifuge fitted with a Beckman SW40Ti rotor (Brea, CA). The temperature was set to 8 °C and the rotor speed to 23,700 rpm (80,000 g). The collected pellet (500−700 μL) was spread evenly on approximately 35−40 clean glass slides (5.7 × 12 × 0.03 mm^3, Matsunami Trading Co., Japan). The samples were allowed to equilibrate at >90% humidity achieved using a K_2SO_4 salt solution. Prior to stacking the slides, the samples were hydrated at 40% by weight using leftover supernatant. The stack was then placed in a glass cell (6 × 20 × 4 mm^3, New Era Enterprises, Inc., Vineland, NJ) that was sealed with beeswax (Hampton Research, Aliso Viejo, CA). Incubation was carried out at 40 °C until clear, at which point the NMR experiments were performed.

NMR Experiments. The solid-state NMR experiments were carried out at the National High Magnetic Field Laboratory (NHMFL, Tallahassee, FL) on a 600 MHz Bruker Avance III spectrometer, with ^{31}P and ^{15}N resonance frequencies of 242.93 and 60.81 MHz. ^{31}P and ^{15}N spectra were referenced to 85% aqueous solution of H_3PO_4 at 0 ppm and ammonium sulfate reference was set to 26.8 ppm, respectively. Prior to data acquisition, the temperature was regulated to the indicated values, which were above the phase transition of the lipids. For ^{31}P, the parameters included a 2 μs pulse (~36° flip-angle) on ^{31}P, a ^{1}H decoupling field of 62.5 kHz during acquisition, a recycle delay of 2 s, and a transient number of 256 scans. The processing involved using 20 Hz of exponential line broadening. For ^{15}N, 2D SAMPI-4 experiments were performed, with parameters including a contact time of 0.81 ms with a ^{1}H spinlock field of ~50 kHz, and a ^{1}H decoupling field of ~62.5 kHz using the phase-wiggled two-pulse phase modulation scheme,[95] a recycle delay of 4.0 s, and 32 t1 increments containing 640−1280 transients each. Processing was done using a Gaussian function (LB = −30 Hz; GB = 0.1).

Molecular Dynamics Simulations. *System Preparation.* Four different membrane compositions were used: 50:25:25 POPC/POPG/16:0 LPC; 50:25:25 POPE/POPG/14:0 LPE; 75:25 POPC/POPG; and 75:25 POPE/POPG. For each of these four membrane compositions, three system types were simulated: peptide-free (control systems), 10 P1 in the top leaflet in an area-matched initial condition (AR systems), and 10 P1 in the top leaflet of a bilayer with equal numbers of lipids in both leaflets (AS systems).

All systems were constructed using the CHARMM-GUI Membrane Builder[96−98] with approximate system dimensions of 100 × 100 × 90 Å and 150 mM sodium chloride in the solvent. Since 14:0 LPE is not available in the standard CHARMM force field, systems containing LPE were initially constructed in CHARMM-GUI with 14:0 LPC; then, CHARMM[99] was used to mutate the head groups and generate protein structure files (PSFs) and protein data bank PDB format files. 14:0 LPE was parametrized by analogy to existing CHARMM 14:0 LPC and POPE parameters, using the standardized CHARMM atom types, partial charges, and force field parameters from the lysophospholipid tail and the POPE headgroup.[100]

For both system types with piscidin, 10 replicates of P1 in α-helical conformations were placed in the top leaflet, with the peptides roughly evenly spaced and at random orientations with respect to one another. In these systems, the membranes were constructed with a total of 300 lipids, to fix the P/L to 1:30. For the AR systems, lipids were initially assigned to either leaflet to match the surface area of both leaflets, while the AS

https://doi.org/10.1021/acs.jpcb.4c05845
J. Phys. Chem. B 2025, 129, 210−227

Table 1. Summary of MD Simulations[a]

system type	lipid composition	lipids/leaflet (top/bottom)	L_{XY} (Å)	equilibration protocol	production MD
peptide-free (control)	0.5:25:25 POPC/POPG/16:0 LPC	176/176	104.82	energy minimization only	1 μs (OpenMM)
	0.75:0.25 POPC/POPG	152/152	101.48		
	0.5:25:25 POPE/POPG/14:0 LPE	184/184	102.40		
	0.75:0.25 POPE/POPG	168/168	102.39		
area relaxed (AR)	0.5:25:25 POPC/POPG/16:0 LPC	133/167	101.45	250 ns (OpenMM) + 50 ns $P2_1$ (CHARMM)	20 μs (Anton 2)
	0.75:0.25 POPC/POPG	134/166	105.94		
	0.5:25:25 POPE/POPG/14:0 LPE	131/169	99.20		
	0.75:0.25 POPE/POPG	129/171	102.87		
area stressed (AS)	0.5:25:25 POPC/POPG/16:0 LPC	150/150	101.80	250 ns (OpenMM)	5 μs (Anton 2)
	0.75:0.25 POPC/POPG	150/150	106.30		
	0.5:25:25 POPE/POPG/14:0 LPE	150/150	99.06		
	0.75:0.25 POPE/POPG	150/150	103.29		

[a]The lipid distributions given for AR systems are after $P2_1$ equilibration, and equilibrium edge dimensions of the simulation cell are calculated from the last 1 μs of production MD (L_{XY}).

systems simply contained 150 lipids in each leaflet. The P1 C-termini were amidated for consistency with the experiments, and all histidine residues were modeled in the neutral state consistent with the measured pK_a values.[67] All simulations utilized the CHARMM 36 force field[100,101] and TIP3P water.[102,103]

Simulations. Simulations were run using a combination of CHARMM version c41b1,[104] OpenMM version 7.4.1,[99] and Anton 2 software version 1.57.1c7.[105] The peptide-free control simulations were simulated for 1 μs in OpenMM. Systems containing peptides were first equilibrated for 250 ns in OpenMM before being moved to Anton 2 for production MD. For the AR systems, an additional equilibration step was performed before running on Anton 2; these systems were simulated for 50 ns in CHARMM using $P2_1$ boundary conditions[84] to allow lipids to equilibrate between leaflets and further reduce the area stress between leaflets.[106] The number of lipids per leaflet was averaged over the last 30 ns of these $P2_1$ simulations, and representative frames with lipid distributions matching this average were then selected as starting coordinates for simulation on Anton 2. While the leaflet lipid ratios post-$P2_1$ did differ slightly from their initial ratios, in most cases the leaflet ratios varied from the ideal 50:25:25 or 75:25 by only 1−2 lipids; Table S4 gives the exact leaflet compositions before and after $P2_1$ equilibration. Production simulations of 5 μs for each AS system and 20 μs for each AR system were carried out on Anton 2. See Table 1 for an overview of the simulation packages, lengths, and equilibration techniques used for each system.

All OpenMM simulations were performed at 310 K and 1 atm with the Monte Carlo membrane barostat[107] and the Nosé−Hoover[108−110] velocity Verlet integrator implemented in *openmmtools*[111] with a collision frequency of 50 ps^{-1}. Bonds with hydrogen were constrained using the SETTLE and CCMA algorithms.[112,113] CHARMM simulations were also run at 310 K and 1 atm, with the Langevin piston barostat and Nosé−Hoover thermostat, a piston mass of 1000 amu and a thermal piston mass of 5000 kcal ps^2; $P2_1$ boundary conditions were used to allow lipids to switch leaflets, with a harmonic restraint applied to all peptides to ensure they remained in the correct leaflet. For both CHARMM and OpenMM simulations, a 12 Å cutoff was used, with a force-switching function from 8 to 12 Å, and long-range electrostatics were treated using the particle mesh Ewald method.[114] Coordinates and velocities were saved every 50 ps in the OpenMM simulations. Simulations on Anton 2 utilized the Multigrator framework[115] with the Nose-Hoover thermostat (310 K, 1 atm) and semi-isotropic MTK barostat. An 8 Å cutoff distance was used, and long-range electrostatics were evaluated with the u-series method[105] Coordinates were saved every 200 ps.

Simulation Analysis. All system snapshots were rendered using VMD.[116] Peptide−lipid radial distribution functions were calculated with LOOS.[117] Water density distribution profiles were calculated using the density function in *cpptraj*[118] with a bin width of 0.5 Å. The PMF (potential of mean force), $F(z)$, was calculated from the normalized water density distribution, $p(z)$:

$$F(z) = -k_B T \ln(p(z)) \tag{3}$$

where k_B is Boltzmann's constant and T is the temperature. Monolayer torque densities, $F'_m(0)$, were calculated from the lateral pressure profile $p(z)$ as described by Park et al.,[106] which were obtained using a developmental version of CHARMM. For a flat membrane with no area strain, the monolayer torque density $F'_m(0)$ is related to the monolayer spontaneous curvature $c_{0,m}$ and is calculated from the first moment of the lateral pressure profile:[106,119]

$$-\int_0^{L/2} zp(z)\mathrm{d}z = F'_m(0) = -K_{c,m}c_{0,m} \tag{4}$$

where L is the system size along the bilayer normal z, $p(z) = p_T(z) - p_N$ is the lateral pressure profile with tangential (p_T) and normal (p_N) components, and $K_{c,m}$ is the monolayer bending modulus.

Cis (pepide-containing) leaflet surface maps and bilayer thickness maps were calculated using the MEMBPLUGIN[120] tool in VMD. The carbonyl carbon atoms in each leaflet were used to define the surface with 5 Å grid spacing. Maps were calculated for each frame of the Anton 2 trajectories and every 200 ps for the control simulations to ensure equal sampling between systems. Three properties were calculated from each map: the average value of the thickness map (i.e., the average thickness); the minimum value of the thickness map (minimum thickness); and the largest positional deviation of

https://doi.org/10.1021/acs.jpcb.4c05845
J. Phys. Chem. B 2025, 129, 210−227

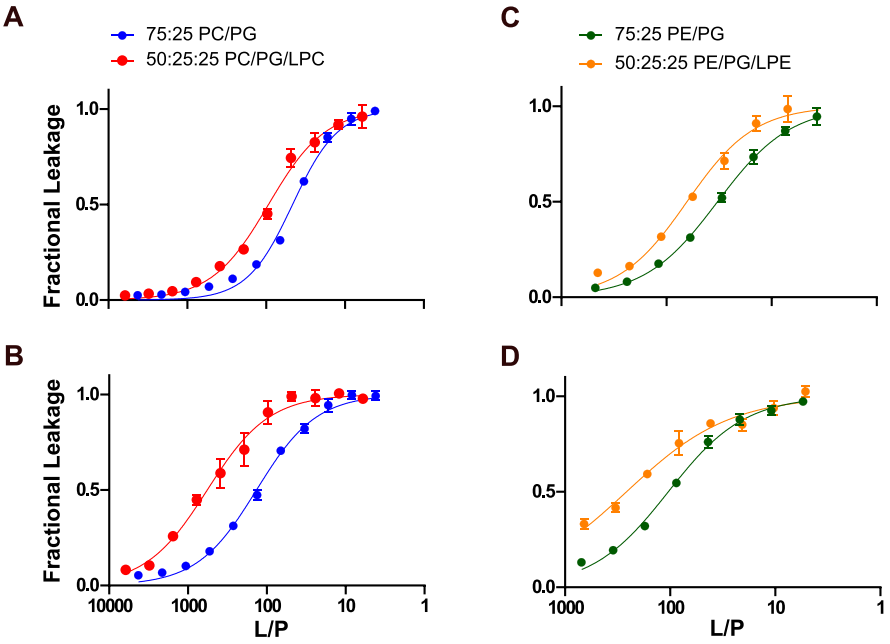

Figure 1. Calcein release curves of P1 and P1−Cu^{2+} acting on membranes with and without LPLs. (A,B) The permeabilization capabilities of P1 (A) and P1−Cu^{2+} (B) were measured on vesicles made of 75:25 POPC/POPG (blue) and 50:25:25 POPC/POPG/16:0 LPC (red). Multiple independent triplicates (n) were run (n = 9 for P1; n = 3 for P1−Cu^{2+}). (C,D) The same measurements were made for P1 (C) and P1−Cu^{2+} (D) acting on vesicles made of 75:25 POPE/POPG (green) and 50:25:25 POPE/POPG/14:0 LPE (yellow). Three independent triplicates (n = 3) were run for the apo and holo states. Each curve corresponds to one representative replicate, and each data point represents the average of fluorescence measurements made in 3 wells, with the error bar corresponding to the standard deviation. Where the error bars are not visible, they are smaller than the marker.

the top leaflet in the direction of the bilayer midplane (maximum leaflet deviation). For the leaflet surface map, the average position of the leaflet is set to 0; deviations away from the bilayer midplane have positive values, and deviations toward the bilayer midplane have negative values.

These maps were used to identify defects. A defect was defined as a bin where there was both significant thinning and a large invagination of the top leaflet; i.e., both the thickness and top leaflet deviation in that bin were less than the specified cutoff. The cutoff values used were 12.2 Å for the thickness and −11.3 Å for the leaflet deviation; these values were chosen as three standard deviations from the population mean for thickness and two standard deviations from the mean for leaflet deviation. Defect frames that were within 10 ns and 10 Å of another identified defect frame were considered separate occurrences of the same defect. Defect lengths were defined as the time in ns between the first occurrence of a defect and its final detection. Defects which were present for only a single frame of the trajectory were assigned a length of 0.

RESULTS

Experimental Data. *Calcein Release from Lysophsopholipid-Containing Vesicles Exposed to P1 Apo and Holo.* Calcein leakage assays were conducted to determine the influence of LPLs on the permeabilization capability of P1. Two LPLs varying in curvature propensity were added to bilayers mimicking bacterial cell membranes. More specifically, we used 16:0 LPC which has a higher positive curvature than 14:0 LPE. The dichain membranes for these respective LPLs were 75:25 POPC/POPG and 75:25 POPE/POPG. To keep the anionic content at 25%, only the zwitterionic lipid (i.e., POPC or POPE), in the host membrane was replaced by the LPL.

Figure 1A,B shows the dye leakage response curves obtained for P1 and P1−Cu^{2+} acting on 75:25 POPC/POPG and 50:25:25 POPC/POPG/16:0 LPC. P1 exhibits the expected behavior as a MAP: the curves are sigmoidal, an indication that a cooperative process is at play.[121] Fitting of each dose−response curve yields the EC_{50} value, which is used to characterize the lipid-to-peptide ratio (L/P) at which 50% of the trapped calcein is released. Table S1 compiles EC_{50} obtained for P1 and P1−Cu^{2+}. Higher EC_{50} values reported as L/P ratios correlate with stronger peptide activity. In POPC/POPG, the EC_{50} values obtained with P1 (40.3 ± 2.5) and P1−Cu^{2+} (107 ± 17) confirm earlier results that metalation enhances membrane activity by more than 2-fold.[73] As shown in Figure 2 and Figure S1, the EC_{50} values increase in a way that is statistically significant when 25% LPC is substituted for POPC. More specifically, we observe an enhancement by factors of 2.3 ($p < 0.05$) and 5.8 ($p < 0.05$) for the EC_{50} of the apo (91.7 ± 7.6) and holo (623 ± 27) states, respectively. Thus, the increased curvature strain associated with the addition of LPC correlates with the enhanced membrane activity induced by the peptides.

When the leakage capabilities of P1 and P1−Cu^{2+} were compared in 75:25 POPE/POPG and 50:25:25 POPE/POPG/14:0 LPE, similar trends were observed albeit with larger error bars compared to the POPC/POPG dichain system (Figure 1C,D). As shown in Figure 2 and Table S1, the EC_{50} of the apo state, which was 31.3 ± 0.9 in 75:25 POPE/POPG increased 2.1 fold ($p < 0.05$) to 65.2 ± 4.5. For the holo-state, the error was significant enough that the apparent increase in EC_{50} did not translate into a statistically significant difference (Figure S1). To test whether the larger error was related to a decrease in bilayer stability and more stochastic permeabilizing events at higher LPE content, we also

https://doi.org/10.1021/acs.jpcb.4c05845
J. Phys. Chem. B 2025, 129, 210−227

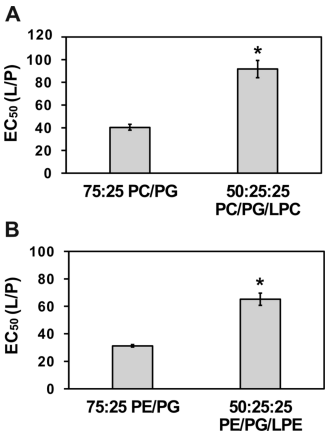

Figure 2. Comparison of EC_{50} values obtained for P1 in the presence and absence of LPLs. (A) The histogram displays the EC_{50} for P1 acting on 75:25 POPC/POPG versus 50:25:25 POPC/POPG/16:0 LPC vesicles. (B) The same as (A) but for the comparison between 75:25 POPE/POPG and 75:25:25 POPE/POPG/14:0 LPE. The error bars correspond to the S.E.M. The corresponding dose−response curves are shown in Figure 1. The asterisks directly above the bars indicate significance ($p < 0.05$) between the LPL-containing system and the dichain membrane.

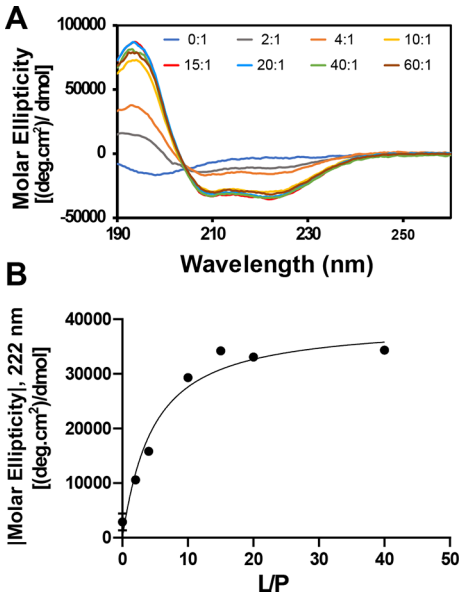

Figure 3. CD-monitored titration of P1 binding to LPL-containing bilayers. (A) The molar ellipticity obtained for P1 added to 50:25:25 POPC/POPG/16:0 LPC vesicles is plotted as a function of the wavelength for a representative replicate. The curves were obtained at increasing L/P ratios, as indicated. The peptide, which is unstructured in the buffer, becomes α-helical when it binds the lipids. (B) The ellipticity at 222 nm was extracted to generate a Langmuir binding isotherm and yield the dissociation constant, K_D. The data from two replicates ($n = 2$) were fitted based on the least-squares method in GraphPad Prism, yielding $K_D = 80.3 \pm 16.7$ μM. A similar value was obtained for P1-Cu^{2+} in POPC/POPG/16:0 LPC (Figure S3). In panel (B), the error bars are not visible because they are smaller than the marker.

investigated POPE/POPG/14:0 LPE systems with lower levels of 14:0 LPE. As shown in Table S1 and Figure S2, we observed that the presence of 15% LPE also significantly ($p < 0.05$) boosts the activities of the apo and holo states.

Overall, the dye leakage results demonstrate that 16:0 LPC and 14:0 LPE increase the membrane activity of P1. The stronger effects obtained with 16:0 LPC correlate with the higher propensity of this LPL to induce positive curvature strain. As a result, we focused on the interactions of P1 with the LPC system as part of the CD and NMR experiments presented next.

Circular Dichroism-Monitored Titration Curves. A CD-monitored titration was performed to determine K_D, the binding dissociation constants of the peptide to 50:25:25 POPC/POPG/16:0 LPC. The procedure was previously used to obtain the K_D in 75:25 POPC/POPG.[73] It is based on the knowledge that P1, which is unstructured in buffer, folds into an α-helical structure in the presence of lipid vesicles.[48,51,73] Figure 3A shows the α-helix bands that build up at 208 and 222 nm when a fixed amount of P1 (20 μM) is titrated with increasing amount of LUVs and the L/P ratio is increased.[73] The two-state behavior of P1 translates into titration curves that cross at a common isosbestic point. As displayed in Figure 3B, the molar ellipticity values observed at 222 nm were used to build a Langmuir binding isotherm that was fitted to yield $K_D = 80.3 \pm 16.7$ μM. This value is on the same order as the K_D of 91 μM previously reported for the dichain membrane.[73] Within the experimental error (assuming similar error for the dichain and LPL-containing membranes), the presence of the LPL does not appear to improve the membrane affinity of the peptide.

^{31}P NMR. To better understand the mechanism of P1 interacting with LPL-containing membranes, we prepared mechanically aligned phospholipid bilayers and recorded their ^{31}P chemical shifts by solid-state NMR. These are excellent reporters of bilayer and nonbilayer states.[122−128] P1 was previously studied in 75:25 POPC/POPG.[48,51,67,74,75] Here, we incorporated P1 at P/L = 1:60 in 50:25:25 POPC/POPG/16:0 LPC, as shown in Figure 4. In the bilayer state, oriented phospholipids give rise to sharp signals near 30 ppm, as it is the case in Figure 4. Based on previous studies done with POPC and POPG,[73] we can readily assign the downfield signal at 27.8 ppm in the 50:25:25 POPC/POPG/16:0 LPC sample to POPC, while POPG resonates at 26.1 ppm. The signal at 20.2 ppm can be assigned to 16:0 LPC,[19,65] confirming that the LPL

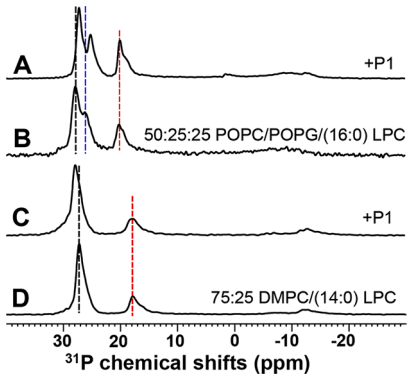

Figure 4. ^{31}P Solid-state NMR spectra of LPL-containing membranes in the absence and presence of P1. Aligned bilayers were made using the indicated lipids in the absence (B,D) and presence of P1 at P/L = 1:60 (A,C). The blue and black dashed lines mark the POPG and POPC (DMPC) signals in the neat bilayers, respectively, while the red line indicates the LPL. The ^{1}H decoupled spectra were collected at $T = 305$ K on a Bruker 600 MHz spectrometer at the NHMFL.

https://doi.org/10.1021/acs.jpcb.4c05845
J. Phys. Chem. B 2025, 129, 210−227

was successfully incorporated into aligned membranes. Upon addition of P1, the phospholipid headgroups interact with the charged peptide. This interaction alters the membrane surface charge and forces the headgroups to move and adopt a new dipole orientation with respect to the bilayer normal, which can translate into chemical shift changes.[48,51,67,74,75] Under the conditions tested, the main change upon P1 addition is the upfield movement of the POPG signal from 27.8 to 25.2 ppm and the rearrangement of the 16:0 LPC signal into a sharp signal at 20.0 ppm and broad shoulder centered near 18.6 ppm. This suggests that P1 influences not only POPG but also the LPL. In DMPC/14:0 LPL, the changes are more subtle, possibly due to a different location of the peptide in the zwitterionic membrane. Micellar states are not detected at 0 ppm but the slightly raised baseline near 16 ppm points at unoriented lipids, suggesting some disruptive effects by P1. In the case of DMPC/14:0 LPC, we did not detect any major change in line width or chemical shift to the LPC signal upon peptide addition. It is possible that the peptide inserts more deeply in the purely zwitterionic membrane, resulting in less drastic changes in the headgroup region. Overall, the ^{31}P NMR data demonstrate the successful incorporation of 16:0 LPC in the POPC/POPG dichain membrane and that the membranes maintain strong alignment in the presence of P1 at P/L = 1:60, thereby enabling the structural characterization of the peptide by ^{15}N NMR, as covered next.

^{15}N NMR. To characterize the conformation of P1 in the presence of LPC and LPE lipids, ^{15}N/^{1}H 2D spectra were collected for the peptide ^{15}N-labeled at different amide positions. As shown in Figure 5, these spectra yield ^{15}N chemical shifts and ^{15}N−^{1}H dipolar interactions. These NMR restraints are excellent indicators of how the peptide is oriented with respect to the bilayer normal; if collected over the full length of the peptide, they can be used to solve the backbone structure at high resolution.[129,130] The structure of P1 has previously been solved in multiple lipid systems, including 75:25 DMPC/DMPG, where DMPG is 1,2-dimyristoyl-*sn*-glycero-3-phosphoglycerol).[50,51] Here, we used the same spectroscopic approach to investigate whether the addition of LPC could change the orientation of the peptide. Figure 5A compares the 2D data for ^{15}N-[$V_{10}G_{13}I_{16}$] P1 in 50:25:25 POPC/POPG/16:0 LPC, 50:25:25 POPE/POPG/14:0 LPE and 75:25 DMPC/14:0 LPC. Figure 5B displays the data collected for four multiply labeled P1 peptides in 75:25 POPC/16:0 LPC, yielding 9 pairs of restraints: I_5, F_6, G_8, V_{10}, V_{12}, G_{13}, I_{16}, L_{19}, and V_{20}. ^{31}P spectra document that the bilayers are well aligned in these samples (Figure 4 and Figure S4). Tables S2 and S3 summarize the ^{15}N chemical shifts and ^{15}N−^{1}H dipolar interactions that were extracted from these spectra. Overall, the features of P1 in 75:25 DMPC/DMPG are well conserved in the LPL systems.[51,74,75,131,132] While PO chains could create a hydrophobic mismatch that prevents the peptide from inserting, no change in orientation is observed when shorter DM chains are used. With ^{15}N chemical shifts centered on 75 ppm, P1 is found to behave as an α-helix that lies parallel to the membrane surface, the so-called surface-bound state (S-state). This is the case even when the anionic PG that could retain the peptide in the headgroup region is removed and the peptide experiences a drastic enhancement in EC_{50} (Table S1 and Figure S5). As previously described in LPL-free bilayers, the peptide appears to permeabilize the LPL-containing membranes by remaining in the S-state and forming transient surface-bound membrane defects.[67,68]

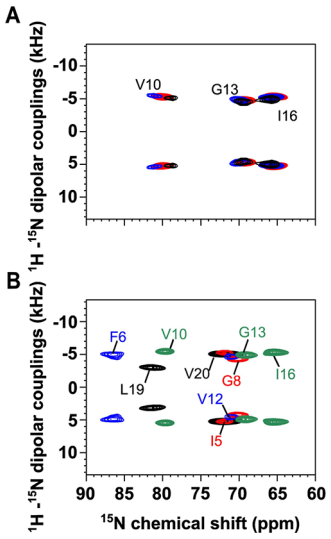

Figure 5. ^{15}N Solid-state NMR spectra of P1 incorporated into LPL-containing bilayers. ^{15}N-Labeled piscidin peptides were incorporated into LPL-containing membranes, and the ^{1}H/ ^{15}N SAMPI-4 spectra[133] were collected at 305 K on a Bruker 600 MHz instrument at the NHMFL. (A) ^{15}N-[$V_{10}G_{13}I_{16}$] P1 in 50:25:25 POPC/POPG/16:0 LPC (red), 50:25:25 POPE/POPG/14:0 LPE (blue), and 75:25 DMPC/14:0 LPC (black). For I_{16} (G_{13}), blue and red (black) signals overlap almost completely. (B) Spectra from four different labeled P1 peptides are compared in 75:25 POPC/16:0 LPC: ^{15}N-[$F_2I_5G_8$] P1 (red), ^{15}N-[F_6V_{12}] P1 (blue), ^{15}N-[$V_{10}G_{13}I_{16}$] P1 (green), and ^{15}N-[$L_{19}V_{20}$] P1 (black). A signal is lacking from F_2 signal due to its location at the amino end where the helix is frayed. Tables S2 and S3 provide the list of observed ^{15}N chemical shifts and ^{15}N−^{1}H dipolar splittings.

Molecular Dynamics Simulations. *Effects of Lysophospholipid on Peptide-Free Systems.* The presence of either 14:0 LPE or 16:0 LPC imparted flexibility and increased fluidity to the membranes simulated, consistent with previous simulation results with 18:1 LPC.[62] This was observed through both a marked thinning of the hydrophobic thickness when 16:0 LPC or 14:0 LPE is present, in addition to greater undulations of the leaflets (Table 2). For the PC-containing membranes, the presence of 25% 16:0 LPC decreased the hydrophobic thickness by ∼1.4 Å, from 27.0 to 25.6 Å, and increased the magnitude of the largest leaflet positional fluctuation by around 0.5 Å, indicating greater surface fluctuations. The results were similar for LPE in the PE-containing systems: the addition of 25% 14:0 LPE thinned the hydrophobic thickness by 1.8 Å (29.1 to 27.3 Å) and increased the largest leaflet positional deviation by 0.3 Å.

This thinning is accompanied by greater hydration and water penetration into the bilayer, as evidenced by the slight decrease in water PMF barrier height and narrowing of the PMF when LPLs of either type are included (Figure 6, dotted lines). In both cases, the decrease of the barrier height is small when LPL is included; the maximum values of the PMFs are 6.5 kcal/mol for both POPC/POPG and POPE/POPG, and 6.4 kcal/mol for the corresponding systems with LPL. The change in the width of the PMFs, however, is much more pronounced. The full width at half-maximum (fwhm) decreases from 16.6 to 14.2 Å when 25% 16:0 LPC is included in the PC-containing system, and decreases from 19.1 to 16.7 Å when 25% 14:0 LPE is included in the PE-containing system.

https://doi.org/10.1021/acs.jpcb.4c05845
J. Phys. Chem. B 2025, 129, 210−227

Table 2. Average Bilayer Properties for All 12 Systems Simulated

system	average thickness (Å)	SE	average minimum thickness (Å)	SE	ave. max leaflet deviation (Å)	SE
PC/PG/16:0 LPC (control)	25.57	0.01	18.89	0.02	−6.05	0.02
PE/PG/14:0 LPE (control)	27.29	0.01	20.84	0.02	−5.94	0.02
PC/PG (control)	26.98	0.01	20.78	0.02	−5.52	0.02
PE/PG (control)	29.08	0.01	22.94	0.02	−5.64	0.02
PC/PG/16:0 LPC (AR)	24.83	<0.01	17.50	<0.01	−7.64	<0.01
PE/PG/14:0 LPE (AR)	25.34	<0.01	17.86	<0.01	−7.72	<0.01
PC/PG (AR)	25.87	<0.01	18.45	<0.01	−7.46	<0.01
PE/PG (AR)	26.82	<0.01	19.48	<0.01	−7.35	<0.01
PC/PG/16:0 LPC (AS)	24.68	<0.01	16.36	0.01	−9.14	0.01
PE/PG/14:0 LPE (AS)	25.23	<0.01	16.60	0.01	−9.59	0.01
PC/PG (AS)	25.43	<0.01	17.12	0.01	−8.99	0.01
PE/PG (AS)	26.54	<0.01	17.98	0.01	−9.25	0.01

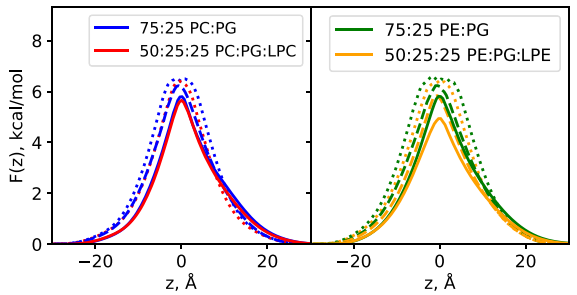

Figure 6. Free energy $F(z)$ for water as a function of the position along the membrane normal. The bilayers are constituted of 50:25:25 POPC/POPG/16:0 LPC and 75:25 POPC/POPG, 50:25:25 POPE/POPG/14:0 LPE, and 75:25 POPE/POPG. The PC-containing systems and PE-containing systems are shown separately. z = 0 represents the bilayer midplane. Dotted lines are P1-free control data, dashed lines are AR systems, and solid lines are AS systems.

Finally, the presence of LPL induces a positive change in the spontaneous curvature in both systems (Table 3), consistent

Table 3. Monolayer Spontaneous Curvatures $c_{0,m}$ (Equation 4) for Peptide-Free Systems[a]

system	$F'_m(0)$	$c_{0,m}$ (Å^{-1})	$R_{0,m}$ (Å)	$K_{c,m}$ (kcal/mol)
PC/PG/16:0 LPC	−0.0069	0.00072	1391.3	9.6
PC/PG	0.0462	−0.00481	−207.8	9.6
PE/PG/14:0 LPE	0.0927	−0.00966	−103.6	9.6
PE/PG	0.1551	−0.01616	−61.9	9.6

[a]Monolayer radius of curvature $R_{0,m} = 1/c_{0,m}$; monolayer bending constant $K_{c,m}$ from the bilayer bending constant reported by Venable et al.[134]

with previous experimental[8] and simulation[62] data. Spontaneous curvatures in the lipid-only systems were obtained from the pressure profiles plotted in the top two panels of Figure 7 (profiles for the bilayers with piscidin were not evaluated because peptide-induced undulations overly blurred the locations of critical features). For these calculations, a monolayer bending constant of 9.6 kcal/mol (the monolayer bending constant of POPC for the C36 force field[134]) was used in Equation 4, since it is difficult to estimate bending constants from simulations of lipid mixtures.

Beginning with the general features of the profiles, there is a characteristic maximum at the bilayer midplane arising from chain repulsion, a minimum near the glycerol groups associated with water/hydrocarbon interfacial tension, and a

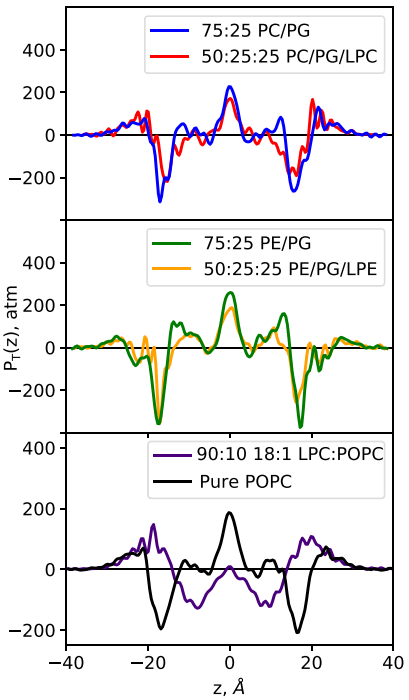

Figure 7. Pressure profiles for bilayers that include LPLs. The bilayers are composed of 50:25:25 POPC/POPG/16:0 LPC and 75:25 POPC/POPG (top), 50:25:25 POPE/POPG/14:0 LPE and 75:25 POPE/POPG (middle), and 9:1 oleoyl-lyso PC (18:1 LPC)/POPC and POPC (from a previous study[62] (bottom)). Statistical errors can be ascertained from the differences in the peak positions between leaflets.

maximum at the phosphate plane from electrostatic repulsion. (See ref[134] for the locations of these planes in assorted homogeneous bilayers generated with the same force field used here.) The bilayers with PE have a minimum not present in PC bilayers at ∼ ± 22 Å arising from hydrogen bonding.[135] This feature in the pressure profile provides a more satisfactory explanation of negative curvature generation by PE headgroups than head/chain "shape" mismatch because lipids in bilayers are constrained to be cylindrical.[134] The pressure profiles of LPL-containing bilayers show systematic differences to the preceding set: the maximum in the bilayer midplane is reduced in size, the relative magnitudes of the other peaks differ, and their average positions shift toward the midplane (consistent with the thinning listed in Table 2). The combination of these changes, which are unevenly distributed along the entire

https://doi.org/10.1021/acs.jpcb.4c05845
J. Phys. Chem. B 2025, 129, 210−227

bilayer, lead to the positive curvature generation by the LPL shown in Table 3. (The features of the 18:1 LPC/POPC profile (bottom panel in Figure 7) are considered in the Discussion.) The pressure profile of the 90:10 18:1 LPC:POPC system (bottom panel) is included for comparison to highlight the features of LPL: higher positive lateral pressure in the phosphate region, nearly zero lateral pressure at the bilayer midplane, and marked thinning of the bilayer.

Proceeding to the details (Table 3), POPE is a negative spontaneous curvature generating lipid, but the presence of 25% LPE decreases the magnitude of this effect from $c_{0,m}$ = −0.0162 to −0.0097 Å^{-1} (corresponding to monolayer radii of spontaneous curvature of −61.9 and −103.6 Å, respectively). In the POPC/POPG membrane, which has a much less negative $c_{0,m}$ to begin with, the addition of 25% LPC is sufficient to change the sign of the leaflet spontaneous curvature from negative to positive: −0.0048 to 0.0007 Å^{-1} (essentially flat).

Effects of Piscidin 1 on Membrane Properties. For all four lipid compositions studied, the presence of 10 P1 at a lipid-to-peptide ratio of 30:1 has a profound impact on the structure of the bilayer. Regardless of the lipid composition, the presence of P1 thins the membrane by ∼1−2 Å, and has an even larger effect on the average minimum thickness, which is reduced by 1.4−5.0 Å (Table 2). For both the average thickness and minimum thickness, the magnitude of the thinning effect of P1 is larger in the LPL-free systems. This may be because LPL also induces thinning, thus the LPL-containing systems already experience a degree of thinning. Despite this, the bilayers with both LPL and P1 are still thinner than their LPL-free counterparts, and are therefore expected to be more permeable to water.

The average thicknesses are not substantially different between AR and AS piscidin distributions. However, the average minimum thickness is impacted by the area stress, with minimum thicknesses 1.1−1.5 Å thinner in AS systems when compared to the corresponding AR systems (Table 2). The bilayer property most impacted by both the presence of P1 and its distribution is the positional deviations of the individual leaflets. In P1-free systems, the average maximum leaflet deviation is around −6 Å, regardless of the membrane type (here, negative values indicate a deviation toward the bilayer midplane). When P1 is added in the AR initial condition, this average value increases in magnitude to around −7.5 Å, and the magnitude increases further to around −9 Å for the AS initial condition (Table 2). Additionally, the probability distributions for all 12 systems (Figure 8) show a striking separation between the control, AR, and AS systems with little separation of the distributions within each grouping. This indicates that the magnitude of leaflet positional fluctuation is almost exclusively influenced by the presence of piscidin and the degree of area stress, rather than the lipid constituents of these membranes.

Additionally, the presence of P1 in either the AR or AS distribution led to increased hydration and water penetration in the bilayer. This is seen through a lowering of the barrier height and narrowing of the peak in the water PMFs calculated for these systems (Figure 6, dotted versus solid curves). In all four membranes studied, this effect is larger with the AS peptide distribution than with the AR distribution. For example, in the 75:25 POPE/POPG membrane, the maximum value of the PMF is 6.5 kcal/mol for the control membrane; the AR piscidin distribution decreases the height by 0.3 kcal/mol to a value of 6.2 kcal/mol, while the AS distribution decreases it by 0.7 to 5.8 kcal/mol. Similar results are observed in the other three membranes studied, though in 50:25:25 POPC/POPG/16:0 LPC the difference between AR and AS is small (5.8 kcal/mol vs 5.7 kcal/mol, respectively).

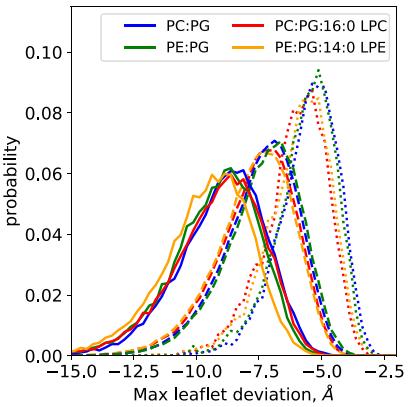

Figure 8. Probability distribution of the maximum leaflet positional deviation for all 12 systems simulated. Dotted lines are P1-free control data, dashed lines are AR systems, and solid lines are AS systems. Negative values indicate deviations in the direction of the bilayer midplane, i.e., deviations that thin the membrane. The magnitudes of leaflet positional deviations are primarily influenced by the presence of P1 and the degree of area stress, rather than the lipid composition of the leaflet.

Defects. Previous simulations of P1 revealed the presence of transient funnel-like defects,[67,68] which were consistent with experimental results showing that piscidin is primarily surface-bound. We hypothesized that the lower EC_{50} values seen experimentally with LPL are indicative of easier/more defect formation in those systems. In this work, a defect is defined as a location in the bilayer where there is both significant thinning and significant invagination of one leaflet (see Methods). While many defects were detected for only a single saved frame of the trajectory, some defects persisted over many frames and could therefore be assigned a length based on the simulation time between the first and final detection of that defect. The number of defects, defect rates (defects/μs), average defect lengths, and percentage of the simulation in which a defect is present are given in Table 4.

The defect rates and likelihoods for both the AR and AS systems followed the same trend as the experimental EC_{50}

Table 4. Defect Counts, Rates, Lengths, and Likelihoods for All Eight Systems with P1 Present[a]

system	defect count	defect rate (μs^{-1})	average defect length (ns)	defect likelihood
PC/PG/16:0 LPC (AR)	72	3.6	2.1 ± 0.8	0.14%
PE/PG/14:0 LPE (AR)	45	2.3	0.6 ± 0.2	0.06%
PC/PG (AR)	26	1.3	0.1 ± 0.1	0.03%
PE/PG (AR)	5	0.3	0.6 ± 0.5	0.01%
PC/PG/16:0 LPC (AS)	111	22.2	2.1 ± 0.5	1.02%
PE/PG/14:0 LPE (AS)	120	24.0	1.6 ± 0.4	0.79%
PC/PG (AS)	55	11.0	0.8 ± 0.3	0.33%
PE/PG (AS)	14	2.8	1.0 ± 0.6	0.08%

[a]Defect length error is the standard error of the mean. Defect likelihood is the percentage of the simulation in which a defect is present.

https://doi.org/10.1021/acs.jpcb.4c05845
J. Phys. Chem. B 2025, 129, 210−227

results, with the highest rates in the 50:25:25 POPC/POPG/16:0 LPC membranes and the lowest in the 75:25 POPC/POPG and 75:25 POPE/POPG membranes. No defects were observed in the control (P1-free) simulations. For all four membranes studied, the defect rates were substantially higher in the AS systems: 8-fold for 75:25 POPC/POPG, 6-fold for 50:25:25 POPC/POPG/16:0 LPC, and approximately 10-fold for both PE-containing membranes. In both the AR and AS systems, defects persist longer on average in the LPL-containing systems than in the corresponding LPL-free ones (Figure S6).

Figure 9 depicts a defect from the 50:25:25 POPC/POPG/16:0 LPC AS system. It is representative of many of the defects

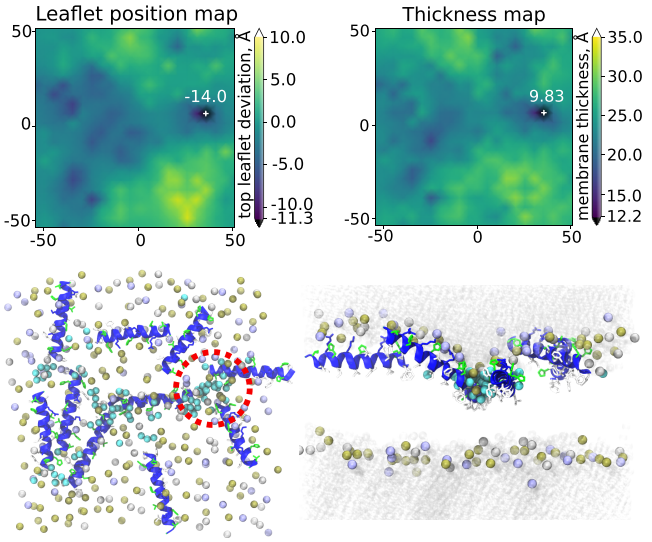

Figure 9. Snapshot of a representative defect from the AS 50:25:25 POPC/POPG/16:0 LPC system. Top panels: top leaflet positional deviation map and bilayer thickness map. Bottom left: top-down view of the system. Bottom right: side view of the system. For the top leaflet positional deviation map, positive values indicate a deviation away from the bilayer midplane and negative values are deviations in the direction of the midplane. For both the leaflet positional map and the thickness map, the minimum value (at the site of the defect) is denoted by a white marker with the value given above. Peptide backbones are shown in blue ribbons; in the side view, basic side chains are blue, polar are green, and apolar white. Phosphate groups from PC are gold, PG silver, and 16:0 LPC lavender. Water molecules within 10 Å of the bilayer midplane are cyan; bulk water is transparent gray in the side view and omitted in the top-down view. Lipid chains (1-palmitate and 2-oleoyl) were omitted for clarity.

observed. The top two panels show the leaflet positional deviation map and bilayer hydrophobic thickness map for this frame of the trajectory. In both maps, the minimum value is indicated by a white marker, with the value of the map at that location printed above it. In this case, the top leaflet invagination is substantial, with a deviation of 14 Å from the average position of the leaflet. Additionally, the bilayer itself is thinned considerably at the site of the defect, with a hydrophobic thickness of only 9.8 Å at that point. Two peptides participate in this defect, and a pocket of water (cyan spheres) is pulled near the bilayer midplane with the peptides and lipid headgroups that make up the defect. Though neither transient pores nor peptide translocation were observed in these simulations, because of the long time scales required, these defects are likely an initial step in the pathway of pore formation and/or peptide translocation, as was recently shown for influenza fusion peptides.[62,136]

DISCUSSION AND CONCLUSIONS

HDPs and LPLs are important biological molecules that exhibit membrane activity and can modulate membrane properties as part of their biological functions. With their broad spectrum activity on dangerous pathogens, HDPs have become promising templates for the design of novel therapeutics to eradicate drug-resistant bacteria.[29,30,36,37,39−42] LPLs, which play multifaceted roles as signaling molecules and constituents of biological membranes, are upregulated in several processes, including bacterial virulence, cancer cell proliferation, and viral envelope biogenesis.[8,13,33,137−139] They have also been investigated for their antimicrobial action.[26,32] To better understand how the combination of HDPs and LPLs influence the integrity of model membranes, we investigated the effects of LPC and LPE on the membrane activity of P1. LPC and LPE are common LPLs found in biological membranes, with LPC producing more curvature strain than LPE.[8] A model HDP, P1 features membrane activity and antimicrobial potency that are positively correlated.[53,140] The thorough biophysical studies that have already been performed on P1 as well as the demonstrated antimicrobial activity of a P1 homologue on *H. pylori*, a bacterium that upregulates LPE in the transition from latent to virulent and exhibits areas of high curvature in its cell wall in relation to its unique helical shape,[141] provide an excellent backdrop to our investigation. Next, we summarize our approach before presenting and discussing the main results. We highlight that the study contributes quantitative and mechanistic knowledge that is relevant to important biological processes where multiple membrane-active agents are implicated.

Featuring experimental and computational tools, we aimed at going beyond the qualitative descriptions that associate positive curvature strain with facilitated peptide insertion. Through dye leakage assays and MD simulations performed on membranes with and without LPLs, we measured how the permeabilization activity of P1 changes as a function of properties that reflect the strength of the membrane permeability barrier, such as the thickness and curvature strain of the membrane and the number of defects it contains. To the best of our knowledge, this is the first study where these properties have been experimentally quantified in the context of combining two different families of membrane-active agents.

Our most significant result is that the enhanced permeabilization potency of P1 observed in the presence of LPLs is underpinned by the ability of the LPLs and peptide to concertedly decrease the membrane thickness; increase the membrane curvature strain, thickness fluctuations and defect formation; and reduce the energy penalty for water penetration in the membrane. The enhancement of peptide activity is stronger with 16:0 LPC than 14:0 LPE (Figures 1 and 2 and Table S1), correlating with the stronger curvature change imposed by LPC. The LPLs alone are insufficient to form pores, as the vesicles studied are stable with the 25% LPL concentration used here. Thus, while the LPLs thin the membrane and increase the amount of water it contains, they do not provide a pathway for water to cross the membrane; P1 is needed to induce permeabilization.

Mechanistically, the MD simulations provide critical insights to explain how P1 achieves enhanced permeabilization in the presence of LPLs. In these simulations, the presence of P1

https://doi.org/10.1021/acs.jpcb.4c05845
J. Phys. Chem. B 2025, 129, 210−227

thins the membrane, increases its hydration, and leads to the formation of defects whether the LPLs are present or not. Adding P1 to the dichain membranes versus the LPL-containing membranes produces a greater net change in these properties, likely because the LPL-containing membranes are already thinned and enriched in water content. Nevertheless, exposed to P1, the LPL-containing membranes attain smaller average thickness and minimum thickness than the dichain membranes. Consistent with the experimental EC_{50} values, P1-induced defect formation is greater in LPL-containing systems; defects occur more frequently and are longer lived when the LPLs are present. The defects formed in the presence of P1 feature the funnel-like structures previously identified in simulations done with the peptide.[50,51,67−69] In order for dye leakage to occur, transient pores must form in the membrane. The defects observed here bear a striking resemblance to fusion peptide pore intermediates,[62] and are likely the first step in the formation of transient pores. A novel feature of our study lies in comparing MD simulations done under two different sets of conditions, area relaxed (AR) and area stressed (AS). Defect rates are higher and longer in duration for AS conditions (Table 4), which is arguably a better model for HDPs on the bacterial membrane surface where the fractional area coverage of the HDP is high, likely inducing high area stress. The differences in the AR and AS conditions and their ramifications will be explored in future work.

As noted in the Introduction, effects of the chain difference of 16:0 LPC and LPE are expected to be minimal on spontaneous curvature. Fuller and Rand[8] provided R_0 for three different LPCs (12:0, 16:0, and 18:1) and LPEs (12:0, 18:0, and 18:1). They found a moderate chain length dependence in R_0 for LPC: 58 Å ($c_0 = 1/R_0 = 0.0172$ Å^{-1}) for 12:0; 68 Å ($c_0 = 0.0147$ Å^{-1}) for 16:0; and 38 Å ($c_0 = 0.0263$ Å^{-1}) for 18;1. Interpolating c_0 for 14:0 yields = 0.0160 Å^{-1}, less than 10% larger than 16:0, a relatively small difference. The experimental values for R_0 of LPEs are all >400 Å, which is nearly flat ($c_0 \approx 0$). Since 14:0 is between 12:0 and 18:0, we can infer that $c_0 \approx 0$ for this as well. In the case of LPEs, the elimination of one chain cancels the negative curvature from the PE headgroup. Similar results are also observed for two-tailed lipids. The experimental radius of curvature R_0 is 28.5 Å for DOPE[142] and 27.5 Å for SDPC.[143] In contrast, R_0 = 87.3 Å for DOPC.[142] Simulations show the same trends, with R_0 of PEs nearly independent of chain length, and qualitatively lower than those of PCs.[134]

The simulations also lend insight to the common assumption that the impact of lipids on membranes can be described by their shape; i.e., the relative volumes of their headgroups and chains. In this model, LPLs are pictured as inverted cones, which is intuitively consistent with their preference for micellular assemblies and ability to destabilize bilayers.[9,11,17,18] It is not clear, however, whether this generally useful qualitative notion could be missing important considerations for LPL action in bilayers. To partly answer this question, begin with the pressure profile of 90:10 14:0 LPC/POPC presented in Figure 7 (bottom). This profile highlights the effects of LPL even though the concentration is extreme (PC vesicles rupture at LPC compositions above 50%).[144] Bilayers of 90:10 18:1 LPC/POPC remained stable in simulations[62] from a combination of time scale and additional stability afforded by periodic boundary conditions. Nevertheless, the 0.0210 Å^{-1} spontaneous curvature of a pure 18:1 LPC bilayer extrapolated from a series of simulations of lower concentrations of 18:1 LPC[62] is sufficiently close to the 0.0263 Å^{-1} obtained experimentally[8] for 18:1 LPC in the inverse hexagonal phase to support further analysis. The positive lateral pressure in the phosphate region in the 90% 18:1 LPC mixture is approximately twice as high as that for pure POPC, and the large positive peak for POPC in the midplane (characteristic for two-chained lipids) is reduced to near zero. These observations are consistent with higher headgroup and lower chain densities as would be pictured by an inverted cone. However, the phosphate maximum and glycerol minimum in the 90% 18:1 LPC mixture have dramatically shifted toward the midplane; i.e., the bilayer has thinned to accommodate the LPL in an environment where lipids are constrained to be more cylindrical. These features were also observed to a lesser extent in the profiles with 25% LPL (Figure 7, top and middle). Hence, lipids adapt to their environment, and the notion that a single shape represents lipids both in isolation and within membranes is misleading. Overall, as already noted in the Results for POPE, the complexity of the pressure profiles and bilayer thinning with LPL demonstrated by our simulations highlight the limitations of shape-based models to quantitatively understand the origin of spontaneous curvature generation in bilayers.

Overall, these observations indicate that LPL increases dye leakage by both imbuing positive leaflet spontaneous curvature, which makes it easier to form pores,[145,146] as well as thinning the membrane and increasing thickness fluctuations, both of which reduce the hydrophobic distance that pores need to span in order to form. We note that the increased number of defects that appear in the presence of the LPLs do not change the binding affinity of the peptide for the membrane, at least within the experimental error associated with the measurement of the K_D by CD (Figure 3). Hence, the mechanism does not seem to involve enhanced membrane interactions mediated by the LPL-induced defects. The ^{31}P solid-state NMR data suggest that LPL interacts with the peptide (Figure 4 and Figure S4), and thus is likely present within the defects. Similar interactions were observed in the MD simulations with P1 having a higher affinity for LPL than any of the other lipids in the systems (Figure S7).

In all lipid systems, including the zwitterionic 16:0 LPC-containing mixtures, the ^{15}N NMR data (Figure 5 and Tables S2 and S3) show that P1 does not adopt the inserted state (I-state) observed for some synthetic MAPs in DMPC/14:0 LPC.[19,65] One possible explanation is that the hydrophobic matching that could be reached with the synthetic peptides within LPL-containing membranes was not achieved for P1 because P1 and the synthetic MAPs are structurally different. For instance, the synthetic MAPs do not contain aromatic residues while P1 has phenylalanine residues that prefer to partition at the water-bilayer interface.[147] As explained above, the I-state is not required for permeabilization as long as transient defects can appear in both leaflets. In the zwitterionic LPC-containing systems where the EC_{50} values are particularly high (Table S1), the number of defects must be more elevated than in the PG-containing membranes. In future work, it would be insightful to use MD to quantify and visualize the defects in these membranes. Like P1, numerous membrane-active HDPs also induce positive curvature strain without forming the I-state.[17,50,66,148,149] Hence, the mechanism highlighted here to explain how LPLs enhance the permeabilization potency of P1 could be relevant to these HDPs, with the prediction that LPLs

https://doi.org/10.1021/acs.jpcb.4c05845
J. Phys. Chem. B 2025, 129, 210−227

will have a similar effect on their mechanism of membrane disruption.

The results obtained here are relevant to biological systems where both MAPs and LPLs are present at the time of biological function. As described in the introduction, *H. pylori*, a bacterium that piscidin is active on, upregulates LPE when it becomes virulent.[56] The specific piscidin, TP4 (FIHHIIGGLFSAGKAIHRLIRRRRR), is very active on this dangerous bacterium, as indicated by minimum inhibitory concentrations that are between 1.5 and 3 μM on different strains.[55] Our results suggest that while bacteria may upregulate LPLs as part of their virulence,[33] host defense mechanisms such as the deployment of membrane-active HDPs could be a benefit bestowed upon the host to counter these bacteria. It is also significant that some LPLs have antimicrobial properties.[26,32,34] Studies characterizing the combined effects of membrane-active agents with antimicrobial properties, as the one presented here, could play an important role in developing novel antimicrobial therapeutics based on the principle of synergy. This would build on ongoing work that is leveraging synergistic antimicrobial activity to eradicate antibiotic-resistant bacteria.[150−152] Synergistic drug combinations have the benefit of reducing the amount of drug needed, resulting in fewer side effects, lower cost, and decreased risk of resistance.

Another important area where LPLs and peptides could converge *in vivo* is in the context of the innate immune response to viral infections. A number of enveloped viruses such as Influenza A contain membranes that are enriched in LPLs compared to dichain membranes.[137,138] P1 is active against a broad range of enveloped viruses, including HIV-1 and SARS-CoV-2.[153−158] Other HDPs are also antiviral.[159−161] Based on our results, we speculate that these peptides experience boosted membrane activity on viral envelopes that are enriched in LPLs. It is also notable that P1 has anticancer activity.[82,162,163] The increased presence of LPLs in cancer cells[139] and concerted disruptive effects with P1 could help enhance the anticancer activity of the peptide. This could be relevant to the mechanism of activity by other anticancer MAPs.[164−168]

In future studies, it would be interesting to quantify how different MAPs respond to the presence of LPLs in membranes mimicking diverse targets, including bacteria, enveloped viruses, and cancer cells. LPLs differing in acyl chain length and headgroup type, and peptide analogs could be screened to determine the specific parameters that determine whether the permeabilization mechanism involves stable or transient pores. These studies could be expanded to MAPs that are involved in fibril formation, such as amyloids, since LPLs can influence fibrillation.[14,169] This information would deepen our mechanistic understanding of how LPLs influence the biological activities of MAPs.

In conclusion, we employed experimental and computational tools to measure the combined effects of two different families of membrane-active agents, HDPs and LPLs. Our results quantify the disruptive effects of the substances on key membrane properties and demonstrate that this translates into a significant increase in permeabilization activity of the peptide. A key message from this study is that peptide activity can be readily modulated by a judicious choice of LPLs. Our study opens the door to more quantitative investigations to characterize how membrane-active agents that perform important biological functions can benefit from each other. With more data, we will improve our ability to predict how to maximize the membrane and antimicrobial activity of MAPs such as P1. Importantly, this could inspire the design of novel antimicrobial formulations based on HDPs, LPLs, and similar membrane-active agents.

■ ASSOCIATED CONTENT

Supporting Information

The Supporting Information is available free of charge at https://pubs.acs.org/doi/10.1021/acs.jpcb.4c05845.

EC_{50} values in different lipid systems; ^{15}N and $^{15}N-^{1}H$ dipolar splittings in different lipid systems; leaflet compositions before and after $P2_1$ equilibration; comparison of EC_{50} values obtained in the presence and absence of LPLs; CD-monitored titration of P1−Cu^{2+} binding to LPC-containing bilayers; ^{31}P spectra of systems with 14:0 LPE or 16:0 LPC in the presence of P1; comparisons of EC_{50} values for P1 and P1−Cu^{2+} in POPC/16:0 LPC; defect lifetime histograms for AR (left) and AS (right) systems (PDF)

■ AUTHOR INFORMATION

Corresponding Authors

Richard W. Pastor − *Laboratory of Computational Biology, National Heart, Lung, and Blood Institute, National Institutes of Health, Bethesda, Maryland 20892, United States;* orcid.org/0000-0002-2454-5131; Email: pastorr@nhlbi.nih.gov

Myriam L. Cotten − *Department of Applied Science, William & Mary, Williamsburg, Virginia 23185, United States; Department of Biochemistry and Biophysics, Oregon State University, Corvallis, Oregon 97331, United States;* orcid.org/0000-0002-6732-1736; Email: cottenmy@oregonstate.edu

Authors

Amy Rice − *Laboratory of Computational Biology, National Heart, Lung, and Blood Institute, National Institutes of Health, Bethesda, Maryland 20892, United States;* orcid.org/0000-0002-7816-8650

Andriana C. Zourou − *Department of Applied Science, William & Mary, Williamsburg, Virginia 23185, United States*

Evan P. Goodell − *Department of Applied Science, William & Mary, Williamsburg, Virginia 23185, United States*

Riqiang Fu − *National High Field Magnetic Laboratory, Tallahassee, Florida 32310, United States;* orcid.org/0000-0003-0075-0410

Complete contact information is available at: https://pubs.acs.org/10.1021/acs.jpcb.4c05845

Author Contributions

△A.R. and A.C.Z. contributed equally. M.L.C., R.W.P, and A.R. conceptualized the overall project. The experimental work was designed by M.L.C., and the experiments were performed and interpreted by M.L.C., R.F., and A.C.Z. The simulations were designed, performed, and analyzed by A.R. and R.W.P. The full draft of the manuscript was arranged by M.L.C., with some sections coming from the coauthors. All coauthors provided feedback on the manuscript.

Notes

The authors declare no competing financial interest.

https://doi.org/10.1021/acs.jpcb.4c05845
J. Phys. Chem. B 2025, 129, 210−227

■ ACKNOWLEDGMENTS

This research was supported by the National Institute of General Medical Sciences (NIH/NIGMS 1 R15 GM126527-01A1 awarded to M.L.C.) and by the Intramural Research Program of the NIH, the National Heart, Lung, and Blood Institute (A.R. and R.W.P.). High-performance computing utilized resources at the National Institutes of Health, Bethesda, MD (NHLBI LoBoS cluster), and the Anton 2 supercomputer. The Anton 2 computer time was provided by the Pittsburgh Supercomputing Center (PSC) through Grant R01GM116961 from the National Institutes of Health. The Anton 2 machine at PSC was generously made available by D. E. Shaw Research. The NMR experiments were performed at the NHMFL supported by the NSF Cooperative agreement (DMR-1644779 and DMR-2128556) and the State of Florida.

■ ABBREVIATIONS

AMPs: antimicrobial peptides
AR: area relaxed
AS: area stressed
ATCUN: amino-terminal copper and nickel (motif)
CD: circular dichroism
Chol: cholesterol
DMPC: 1,2-dimyristoyl-*sn*-glycero-3-phosphocholine
EC_{50}: effective half-maximal concentration
fwhm: full width at half-maximum
HDP: host defense peptide
HEPES: 4-(2-hydroxyethyl)-1-piperazineethanesulfonic acid
HPLC: high-performance liquid chromatography
I-state: inserted state
K_D: dissociation constant
L/P: lipid-to-peptide ratio
LPC: lysophosphatidylcholine
LPE: lysophosphatidylethanolamine
LPL: lysophospholipid
LUVs: large unilamellar vesicles
MAP: membrane-active peptide
MD: molecular dynamics
MWCO: molecular weight cutoff
NHMFL: National High Magnetic Field Laboratory
P1: piscidin 1
PMF: potential of mean force
POPC: 1-palmitoyl-2-oleoyl-glycero-3-phosphocholine
POPE: 1-palmitoyl-2-oleoyl-*sn*-glycero-3-phosphoethanolamine
POPG: 1-palmitoyl-2-oleoyl-*sn*-glycero-3-phospho-(1′-*rac*-glycerol)
S-state: surface-bound state
TFA: trifluoroacetic acid

■ REFERENCES

(1) Arouri, A.; Mouritsen, O. G. Membrane-perturbing effect of fatty acids and lysolipids. *Prog. Lipid Res.* **2013**, *52* (1), 130−40.
(2) Phillips, R.; Ursell, T.; Wiggins, P.; Sens, P. Emerging roles for lipids in shaping membrane-protein function. *Nature* **2009**, *459* (7245), 379−85.
(3) Sanderson, J. M. Peptide-lipid interactions: insights and perspectives. *Org. Biomol Chem.* **2005**, *3* (2), 201−12.
(4) van Meer, G.; Voelker, D. R.; Feigenson, G. W. Membrane lipids: where they are and how they behave. *Nat. Rev. Mol. Cell Biol.* **2008**, *9* (2), 112−24.
(5) Virtanen, J. A.; Cheng, K. H.; Somerharju, P. Phospholipid composition of the mammalian red cell membrane can be rationalized by a superlattice model. *Proc. Natl. Acad. Sci. U. S. A.* **1998**, *95* (9), 4964−9.
(6) Harayama, T.; Riezman, H. Understanding the diversity of membrane lipid composition. *Nat. Rev. Mol. Cell Biol.* **2018**, *19* (5), 281−296.
(7) Kuivenhoven, J. A.; Hegele, R. A. Mining the genome for lipid genes. *Biochim. Biophys. Acta* **2014**, *1842* (10), 1993−2009.
(8) Fuller, N.; Rand, R. P. The influence of lysolipids on the spontaneous curvature and bending elasticity of phospholipid membranes. *Biophys. J.* **2001**, *81* (1), 243−254.
(9) Høyrup, P.; Davidsen, J.; Jørgensen, K. Lipid membrane partitioning of lysolipids and fatty acids: effects of membrane phase structure and detergent chain length. *J. Phys. Chem. B* **2001**, *105* (13), 2649−2657.
(10) Henriksen, J. R.; Andresen, T. L.; Feldborg, L. N.; Duelund, L.; Ipsen, J. H. Understanding detergent effects on lipid membranes: A model study of lysolipids. *Biophys. J.* **2010**, *98* (10), 2199−2205.
(11) Mouritsen, O. G. Lipids, curvature, and nano-medicine. *Eur. J. Lipid Sci. Technol.* **2011**, *113* (10), 1174−1187.
(12) Hisano, Y.; Hla, T. Bioactive lysolipids in cancer and angiogenesis. *Pharmacol. Ther.* **2019**, *193*, 91−98.
(13) Engelbrecht, E.; MacRae, C. A.; Hla, T. Lysolipids in Vascular Development, Biology, and Disease. *Arterioscler. Thromb. Vasc. Biol.* **2021**, *41* (2), 564−584.
(14) Rasmussen, H.; Otzen, D. E.; Pedersen, J. S. Induction, inhibition, and incorporation: Different roles for anionic and zwitterionic lysolipids in the fibrillation of the functional amyloid FapC. *J. Biol. Chem.* **2022**, *298* (2), No. 101569.
(15) Wang, A.; Dennis, E. A. Mammalian lysophospholipases. *Biochim. Biophys. Acta* **1999**, *1439* (1), 1−16.
(16) van den Brink-van der Laan, E.; Antoinette Killian, J.; de Kruijff, B. Nonbilayer lipids affect peripheral and integral membrane proteins via changes in the lateral pressure profile. *Biochim. Biophys. Acta, Biomembr.* **2004**, *1666* (1−2), 275−288.
(17) Koller, D.; Lohner, K. The role of spontaneous lipid curvature in the interaction of interfacially active peptides with membranes. *Biochimica et Biophysica Acta - Biomembranes* **2014**, *1838* (9), 2250−2259.
(18) Grit, M.; Crommelin, D. J. The effect of aging on the physical stability of liposome dispersions. *Chem. Phys. Lipids* **1992**, *62* (2), 113−22.
(19) Strandberg, E.; Bentz, D.; Wadhwani, P.; Ulrich, A. S. Chiral supramolecular architecture of stable transmembrane pores formed by an α-helical antibiotic peptide in the presence of lyso-lipids. *Sci. Rep.* **2020**, *10* (1), 4710.
(20) Jovanović, O.; Chekashkina, K.; Škulj, S.; Žuna, K.; Vazdar, M.; Bashkirov, P. V.; Pohl, E. E. Membrane Lipid Reshaping Underlies Oxidative Stress Sensing by the Mitochondrial Proteins UCP1 and ANT1. *Antioxidants* **2022**, *11* (12), 2314.
(21) Shai, Y. Mode of action of membrane active antimicrobial peptides. *Biopolymers* **2002**, *66*, 236−248.
(22) Ulmschneider, J. P. Charged Antimicrobial Peptides Can Translocate across Membranes without Forming Channel-like Pores. *Biophys. J.* **2017**, *113* (1), 73−81.
(23) Wieprecht, T.; Dathe, M.; Krause, E.; Beyermann, M.; Maloy, W. L.; MacDonald, D. L.; Bienert, M. Modulation of membrane activity of amphipathic, antibacterial peptides by slight modifications of the hydrophobic moment. *FEBS Lett.* **1997**, *417*, 135−140.
(24) Lohner, K. Membrane-active antimicrobial peptides as template structures for novel antibiotic agents. *Curr. Top. Med. Chem.* **2016**, *17* (5), 508−519.
(25) Sani, M. A.; Separovic, F. How membrane-active peptides get into lipid membranes. *Acc. Chem. Res.* **2016**, *49* (6), 1130−8.
(26) Skindersoe, M. E.; Krogfelt, K. A.; Blom, A.; Jiang, G.; Prestwich, G. D.; Mansell, J. P. Dual Action of Lysophosphatidate-Functionalised Titanium: Interactions with Human (MG63) Osteoblasts and Methicillin Resistant Staphylococcus aureus. *PLoS One* **2015**, *10* (11), No. e0143509.

https://doi.org/10.1021/acs.jpcb.4c05845
J. Phys. Chem. B 2025, 129, 210−227

(27) Yan, J.; Wang, K.; Dang, W.; Chen, R.; Xie, J.; Zhang, B.; Song, J.; Wang, R. Two hits are better than one: membrane-active and DNA binding-related double-action mechanism of NK-18, a novel antimicrobial peptide derived from mammalian NK-lysin. *Antimicrob. Agents Chemother.* **2013**, *57* (1), 220−8.
(28) Faust, J. E.; Yang, P.-Y.; Huang, H. W. Action of Antimicrobial Peptides on Bacterial and Lipid Membranes: A Direct Comparison. *Biophys. J.* **2017**, *112* (8), 1663−1672.
(29) Mookherjee, N.; Anderson, M. A.; Haagsman, H. P.; Davidson, D. J. Antimicrobial host defence peptides: functions and clinical potential. *Nat. Rev. Drug Disc.* **2020**, *19* (5), 311−332.
(30) Fjell, C. D.; Hiss, J. A.; Hancock, R. E. W.; Schneider, G. Designing antimicrobial peptides: form follows function. *Nat. Rev. Drug Disc* **2012**, *11* (1), 37−51.
(31) Hancock, R. E. W.; Rozek, A. Role of membranes in the activities of antimicrobial cationic peptides. *FEMS Microbiol. Lett.* **2002**, *206*, 143−149.
(32) McSorley, J. C.; MacFadyen, A. C.; Kerr, L.; Tucker, N. P. Host lysolipid differentially modulates virulence factor expression and antimicrobial susceptibility in Pseudomonas aeruginosa. *Microbiology* **2022**, *168* (7), No. 001179.
(33) Cao, X.; van Putten, J. P. M.; Wösten, M. M. S. M. Chapter Two - Biological functions of bacterial lysophospholipids. In *Advances in Microbial Physiology*, Poole, R. K.; Kelly, D. J., Eds. Academic Press: 2023, Vol. *82*, pp 129−154.
(34) Krogfelt, K. A.; Utley, M.; Krivan, H. C.; Laux, D. C.; Cohen, P. S. Specific phospholipids enhance the activity of beta-lactam antibiotics against Pseudomonas aeruginosa. *J. Antimicrob. Chemother.* **2000**, *46* (3), 377−84.
(35) Magana, M.; Pushpanathan, M.; Santos, A. L.; Leanse, L.; Fernandez, M.; Ioannidis, A.; Giulianotti, M. A.; Apidianakis, Y.; Bradfute, S.; Ferguson, A. L.; et al. The value of antimicrobial peptides in the age of resistance. *Lancet Infect. Dis.* **2020**, *20* (9), e216−e230.
(36) Haney, E. F.; Hancock, R. E. W. Peptide design for antimicrobial and immunomodulatory applications. *Pept. Sci.* **2013**, *100*, 572−583.
(37) Greve, J. M.; Cowan, J. A. Tackling antimicrobial stewardship through synergy and antimicrobial peptides. *RSC Med. Chem.* **2022**, *13* (5), 511−521.
(38) Sheard, D. E.; O'Brien-Simpson, N. M.; Wade, J. D.; Separovic, F. Combating bacterial resistance by combination of antibiotics with antimicrobial peptides. *Pure Appl. Chem.* **2019**, *91* (2), 199−209.
(39) Ruden, S.; Rieder, A.; Chis Ster, I.; Schwartz, T.; Mikut, R.; Hilpert, K. Synergy Pattern of Short Cationic Antimicrobial Peptides Against Multidrug-Resistant Pseudomonas aeruginosa. *Front. Microbiol.* **2019**, *10*, 2740.
(40) Kumar, P.; Kizhakkedathu, J. N.; Straus, S. K. Antimicrobial Peptides: Diversity, Mechanism of Action and Strategies to Improve the Activity and Biocompatibility In Vivo. *Biomolecules* **2018**, *8* (1), 4.
(41) Moreno, M. G.; Lombardi, L.; Di Luca, M. Antimicrobial peptides for the control of biofilm formation. *Curr. Top. Med. Chem.* **2017**, *17*, 1965−1986.
(42) Pearson, C. S.; Kloos, Z.; Murray, B.; Tabe, E.; Gupta, M.; Kwak, J. H.; Karande, P.; McDonough, K. A.; Belfort, G. Combined Bioinformatic and Rational Design Approach To Develop Antimicrobial Peptides against Mycobacterium tuberculosis. *Antimicrob. Agents Chemother.* **2016**, *60* (5), 2757−64.
(43) Wan, F.; Torres, M. D. T.; Peng, J.; de la Fuente-Nunez, C. Deep-learning-enabled antibiotic discovery through molecular de-extinction. *Nat. Biomed. Eng.* **2024**, *8*, 854.
(44) Silphaduang, U.; Noga, E. J. Peptide antibiotics in mast cells of fish. *Nature* **2001**, *414*, 268−269.
(45) Lauth, X.; Shike, H.; Burns, J. C.; Westerman, M. E.; Ostland, V. E.; Carlberg, J. M.; Van Olst, J. C.; Nizet, V.; Taylor, S. W.; Shimizu, C.; et al. Discovery and characterization of two isoforms of moronecidin, a novel antimicrobial peptide from hybrid striped bass. *J. Biol. Chem.* **2002**, *277* (7), 5030−5039.
(46) Campagna, S.; Saint, N.; Molle, G.; Aumelas, A. Structure and mechanism of action of the antimicrobial peptide piscidin. *Biochemistry* **2007**, *46*, 1771−1778.
(47) Lee, S. A.; Kim, Y. K.; Lim, S. S.; Zhu, W. L.; Ko, H.; Shin, S. Y.; Hahm, K.; Kim, Y. Solution structure and cell selectivity of piscidin 1 and its analogues. *Biochemistry* **2007**, *46*, 3653−3663.
(48) Chekmenev, E. Y.; Vollmar, B. S.; Forseth, K. T.; Manion, M. N.; Jones, S. M.; Wagner, T. J.; Endicott, R. M.; Kyriss, B. P.; Homem, L. M.; Pate, M.; et al. Investigating molecular recognition and biological function at interfaces using piscidins, antimicrobial peptides from fish. *Biochim. Biophys. Acta* **2006**, *1758*, 1359−1372.
(49) Hayden, R. M.; Goldberg, G. K.; Ferguson, B. M.; Schoeneck, M. W.; Libardo, M. D.; Mayeux, S. E.; Shrestha, A.; Bogardus, K. A.; Hammer, J.; Pryshchep, S.; et al. Complementary Effects of Host Defense Peptides Piscidin 1 and Piscidin 3 on DNA and Lipid Membranes: Biophysical Insights into Contrasting Biological Activities. *J. Phys. Chem. B* **2015**, *119* (49), 15235−46.
(50) Comert, F.; Greenwood, A.; Maramba, J.; Acevedo, R.; Lucas, L.; Kulasinghe, T.; Cairns, L. S.; Wen, Y.; Fu, R.; Hammer, J.; et al. The host-defense peptide piscidin P1 reorganizes lipid domains in membranes and decreases activation energies in mechanosensitive ion channels. *J. Biol. Chem.* **2019**, *294* (49), 18557−18570.
(51) Perrin, B. S., Jr.; Tian, Y.; Fu, R.; Grant, C. V.; Chekmenev, E. Y.; Wieczorek, W. E.; Dao, A. E.; Hayden, R. M.; Burzynski, C. M.; Venable, R. M.; et al. High-resolution structures and orientations of antimicrobial peptides piscidin 1 and piscidin 3 in fluid bilayers reveal tilting, kinking, and bilayer immersion. *J. Am. Chem. Soc.* **2014**, *136* (9), 3491−3504.
(52) Jiang, Z.; Vasil, A. I.; Vasil, M. L.; Hodges, R. S. ″Specificity Determinants″ Improve Therapeutic Indices of Two Antimicrobial Peptides Piscidin 1 and Dermaseptin S4 Against the Gram-negative Pathogens Acinetobacter baumannii and Pseudomonas aeruginosa. *Pharmaceuticals (Basel)* **2014**, *7* (4), 366−391.
(53) Cetuk, H.; Maramba, J.; Britt, M.; Scott, A. J.; Ernst, R. K.; Mihailescu, M.; Cotten, M. L.; Sukharev, S. Differential Interactions of Piscidins with Phospholipids and Lipopolysaccharides at Membrane Interfaces. *Langmuir* **2020**, *36* (18), 5065−5077.
(54) Oludiran, A.; Malik, A.; Zourou, A. C.; Wu, Y.; Gross, S. P.; Siryapon, A.; Poudel, A.; Alleyne, K.; Adams, S.; Courson, D. S.; et al. Host-defense piscidin peptides as antibiotic adjuvants against Clostridioides difficile. *PLoS One* **2024**, *19* (1), No. e0295627.
(55) Narayana, J. L.; Huang, H. N.; Wu, C. J.; Chen, J. Y. Efficacy of the antimicrobial peptide TP4 against Helicobacter pylori infection: in vitro membrane perturbation via micellization and in vivo suppression of host immune responses in a mouse model. *Oncotarget* **2015**, *6* (15), 12936−54.
(56) Tannaes, T.; Grav, H. J.; Bukholm, G. Lipid profiles of Helicobacter pylori colony variants. *APMIS* **2000**, *108* (5), 349−56.
(57) Vedham, V.; Divi, R. L.; Starks, V. L.; Verma, M. Multiple infections and cancer: implications in epidemiology. *Technol. Cancer Res. Treat.* **2014**, *13* (2), 177−94.
(58) Grage, S. L.; Afonin, S.; Ieronimo, M.; Berditsch, M.; Wadhwani, P.; Ulrich, A. S. Probing and Manipulating the Lateral Pressure Profile in Lipid Bilayers Using Membrane-Active Peptides-A Solid-State (19)F NMR Study. *Int. J. Mol. Sci.* **2022**, *23* (9), 4544.
(59) Israelachvili, J. N.; Mitchell, D. J.; Ninham, B. W. Theory of self-assembly of lipid bilayers and vesicles. *Biochim. Biophys. Acta* **1977**, *470* (2), 185−201.
(60) Cullis, P. R.; de Kruijff, B. Lipid polymorphism and the functional roles of lipids in biological membranes. *Biochim. Biophys. Acta* **1979**, *559* (4), 399−420.
(61) Graham, T. R.; Kozlov, M. M. Interplay of proteins and lipids in generating membrane curvature. *Curr. Opin. Cell Biol.* **2010**, *22* (4), 430−6.
(62) Rice, A.; Zimmerberg, J.; Pastor, R. W. Initiation and evolution of pores formed by influenza fusion peptides probed by lysolipid inclusion. *Biophys. J.* **2023**, *122* (6), 1018−1032.

https://doi.org/10.1021/acs.jpcb.4c05845
J. Phys. Chem. B 2025, 129, 210−227

(63) Lundbaek, J. A.; Andersen, O. S. Lysophospholipids modulate channel function by altering the mechanical properties of lipid bilayers. *J. Gen. Physiol.* **1994**, *104* (4), 645−73.
(64) Burack, W. R.; Dibble, A. R. G.; Allietta, M. M.; Biltonen, R. L. Changes in Vesicle Morphology Induced by Lateral Phase Separation Modulate Phospholipase A2 Activity. *Biochemistry* **1997**, *36* (34), 10551−10557.
(65) Grau-Campistany, A.; Strandberg, E.; Wadhwani, P.; Rabanal, F.; Ulrich, A. S. Extending the Hydrophobic Mismatch Concept to Amphiphilic Membranolytic Peptides. *J. Phys. Chem. Lett.* **2016**, *7* (7), 1116−20.
(66) Perrin, B. S., Jr.; Sodt, A. J.; Cotten, M. L.; Pastor, R. W. The Curvature Induction of Surface-Bound Antimicrobial Peptides Piscidin 1 and Piscidin 3 Varies with Lipid Chain Length. *J. Membr. Biol.* **2015**, *248* (3), 455−67.
(67) Mihailescu, M.; Sorci, M.; Seckute, J.; Silin, V. I.; Hammer, J.; Perrin, B. S., Jr; Hernandez, J. I.; Smajic, N.; Shrestha, A.; Bogardus, K. A.; et al. Structure and Function in Antimicrobial Piscidins: Histidine Position, Directionality of Membrane Insertion, and pH-Dependent Permeabilization. *J. Am. Chem. Soc.* **2019**, *141* (25), 9837−9853.
(68) Perrin, B. S.; Fu, R.; Cotten, M. L.; Pastor, R. W. Simulations of membrane-disrupting peptides II: AMP piscidin 1 favors surface defects over pores. *Biophys. J.* **2016**, *111*, 1258−1266.
(69) Mihajlovic, M.; Lazaridis, T. Antimicrobial peptides bind more strongly to membrane pores. *Biochimica et biophysica acta* **2010**, *1798* (8), 1494−502.
(70) D'Arrigo, P.; Servi, S. Synthesis of lysophospholipids. *Molecules* **2010**, *15* (3), 1354−77.
(71) Cantor, R. S. Lipid composition and the lateral pressure profile in bilayers. *Biophys. J.* **1999**, *76* (5), 2625−39.
(72) Ratledge, C.; Wilkinson, S. G., An overview of microbial lipids. In *Microbial Lipids*, Ratledge, C.; Wilkinson, S. G., Eds. Academic Press: London, 1988; Vol. *1*, pp 3− 22.
(73) Paredes, S. D.; Kim, S.; Rooney, M. T.; Greenwood, A. I.; Hristova, K.; Cotten, M. L. Enhancing the membrane activity of Piscidin 1 through peptide metallation and the presence of oxidized lipid species: Implications for the unification of host defense mechanisms at lipid membranes. *Biochim Biophys Acta Biomembr* **2020**, *1862* (7), No. 183236.
(74) Chekmenev, E. Y.; Jones, S. M.; Nikolayeva, Y. N.; Vollmar, B. S.; Wagner, T. J.; Gor'kov, P. L.; Brey, W. W.; Manion, M. N.; Daugherty, K. C.; Cotten, M. High-field NMR studies of molecular recognition and structure-function relationships in antimicrobial piscidins at the water-lipid bilayer interface. *J. Am. Chem. Soc.* **2006**, *128*, 5308−5309.
(75) Chekmenev, E.; Vollmar, B.; Cotten, M. Can antimicrobial peptides scavenge around a cell in less than a second? *Biochim. Biophys. Acta* **2010**, *1798*, 228−234.
(76) Ramamoorthy, A.; Thennarasu, S.; Lee, D. K.; Tan, A.; Maloy, L. Solid-state NMR investigation of the membrane-disrupting mechanism of antimicrobial peptides MSI-78 and MSI-594 derived from magainin 2 and melittin. *Biophys. J.* **2006**, *91*, 206−216.
(77) Mason, A. J.; Marquette, A.; Bechinger, B. Zwitterionic phospholipids and sterols modulate antimicrobial peptide-induced membrane destabilization. *Biophys. J.* **2007**, *93* (12), 4289−4299.
(78) Sherman, P. J.; Jackway, R. J.; Gehman, J. D.; Praporski, S.; McCubbin, G. A.; Mechler, A.; Martin, L. L.; Separovic, F.; Bowie, J. H. Solution Structure and Membrane Interactions of the Antimicrobial Peptide Fallaxidin 4.1a: An NMR and QCM Study. *Biochemistry* **2009**, *48* (50), 11892−11901.
(79) Kim, S. Y.; Zhang, F.; Gong, W.; Chen, K.; Xia, K.; Liu, F.; Gross, R.; Wang, J. M.; Linhardt, R. J.; Cotten, M. L. Copper regulates the interactions of antimicrobial piscidin peptides from fish mast cells with formyl peptide receptors and heparin. *J. Biol. Chem.* **2018**, *293* (40), 15381−15396.
(80) Libardo, M. D. J.; Bahar, A. A.; Ma, B.; Fu, R.; McCormick, L. E.; Zhao, J.; McCallum, S. A.; Nussinov, R.; Ren, D.; Angeles-Boza, A. M.; et al. Nuclease activity gives an edge to host-defense peptide piscidin 3 over piscidin 1, rendering it more effective against persisters and biofilms. *FEBS J.* **2017**, *284* (21), 3662−3683.
(81) Fu, R.; Rooney, M. T.; Zhang, R.; Cotten, M. L. Coordination of Redox Ions within a Membrane-Binding Peptide: A Tale of Aromatic Rings. *J. Phys. Chem. Lett.* **2021**, *12* (18), 4392−4399.
(82) Comert, F.; Heinrich, F.; Chowdhury, A.; Schoeneck, M.; Darling, C.; Anderson, K. W.; Libardo, M. D. J.; Angeles-Boza, A. M.; Silin, V.; Cotten, M. L.; et al. Copper-binding anticancer peptides from the piscidin family: an expanded mechanism that encompasses physical and chemical bilayer disruption. *Sci. Rep.* **2021**, *11* (1), 12620.
(83) Rai, R. K.; De Angelis, A.; Greenwood, A.; Opella, S. J.; Cotten, M. L. Metal-ion Binding to Host Defense Peptide Piscidin 3 Observed in Phospholipid Bilayers by Magic Angle Spinning Solid-state NMR. *ChemPhysChem* **2019**, *20* (2), 295.
(84) Dolan, E. A.; Venable, R. M.; Pastor, R. W.; Brooks, B. R. Simulations of Membranes and Other Interfacial Systems Using P2(1) and Pc Periodic Boundary Conditions. *Biophys. J.* **2002**, *82* (5), 2317−2325.
(85) Rice, A.; Prasad, S.; Brooks, B. R.; Pastor, R. W. Simulating asymmetricmembranes using P21 periodic boundary conditions. In *Methods in Enzymology*, Deserno, M.; Baumgart, T., Eds. Academic Press: 2024, Vol. *701*, pp 309−358.
(86) Gasmi, G.; Singer, A.; Forman-Kay, J.; Sarkar, B. NMR structure of neuromedin C, a neurotransmitter with an amino terminal CuII-, NiII-binding (ATCUN) motif. *J. Pept. Res.* **1997**, *49* (6), 500−9.
(87) Chen, P. S.; Toribara, T. Y.; Warner, H. Microdetermination of Phosphorus. *Anal. Chem.* **1956**, *28* (11), 1756−1758.
(88) King, E. J. The colorimetric determination of phosphorus. *Biochem. J.* **1932**, *26* (2), 292−7.
(89) Sani, M. A.; Gagne, E.; Gehman, J. D.; Whitwell, T. C.; Separovic, F. Dye-release assay for investigation of antimicrobial peptide activity in a competitive lipid environment. *Eur. Biophys. J.* **2014**, *43* (8−9), 445−450.
(90) Yang, J. T.; Wu, C. S.; Martinez, H. M. Calculation of protein conformation from circular dichroism. *Methods Enzymol* **1986**, *130*, 208−69.
(91) Corrêa, D. H.; Ramos, C. H. The use of circular dichroism spectroscopy to study protein folding, form and function. *Afr. J. Biochem. Res.* **2009**, *3* (5), 164−173.
(92) Duarte, A. M.; Wolfs, C. J.; van Nuland, N. A.; Harrison, M. A.; Findlay, J. B.; van Mierlo, C. P.; Hemminga, M. A. Structure and localization of an essential transmembrane segment of the proton translocation channel of yeast H+-V-ATPase. *Biochimica et biophysica acta* **2007**, *1768* (2), 218−27.
(93) Fujiwara, Y.; Kurokawa, T.; Takeshita, K.; Kobayashi, M.; Okochi, Y.; Nakagawa, A.; Okamura, Y. The cytoplasmic coiled-coil mediates cooperative gating temperature sensitivity in the voltage-gated H(+) channel Hv1. *Nat. Commun.* **2012**, *3*, 816.
(94) Greenfield, N. J. Using circular dichroism spectra to estimate protein secondary structure. *Nat. Protoc* **2006**, *1* (6), 2876−90.
(95) Fu, R. Efficient heteronuclear dipolar decoupling in NMR of static solid samples using phase-wiggled two-pulse phase modulation. *Chem. Phys. Lett.* **2009**, *483* (1), 147−153.
(96) Jo, S.; Kim, T.; Iyer, V. G.; Im, W. CHARMM-GUI: A web-based graphical user interface for CHARMM. *J. Comput. Chem.* **2008**, *29* (11), 1859−1865.
(97) Jo, S.; Lim, J. B.; Klauda, J. B.; Im, W. CHARMM-GUI Membrane Builder for Mixed Bilayers and Its Application to Yeast Membranes. *Biophys. J.* **2009**, *97* (1), 50−58.
(98) Wu, E. L.; Cheng, X.; Jo, S.; Rui, H.; Song, K. C.; Dávila-Contreras, E. M.; Qi, Y.; Lee, J.; Monje-Galvan, V.; Venable, R. M.; et al. CHARMM-GUI Membrane Builder toward realistic biological membrane simulations. *J. Comput. Chem.* **2014**, *35* (27), 1997−2004.
(99) Eastman, P.; Swails, J.; Chodera, J. D.; McGibbon, R. T.; Zhao, Y.; Beauchamp, K. A.; Wang, L.-P.; Simmonett, A. C.; Harrigan, M. P.; Stern, C. D.; et al. OpenMM 7: Rapid development of high

performance algorithms for molecular dynamics. *PLOS Computational Biology* **2017**, *13* (7), No. e1005659.
(100) Klauda, J. B.; Venable, R. M.; Freites, J. A.; O'Connor, J. W.; Tobias, D. J.; Mondragon-Ramirez, C.; Vorobyov, I.; MacKerell, A. D., Jr; Pastor, R. W. Update of the CHARMM All-Atom Additive Force Field for Lipids: Validation on Six Lipid Types. *J. Phys. Chem. B* **2010**, *114* (23), 7830−7843.
(101) Huang, J.; Rauscher, S.; Nawrocki, G.; Ran, T.; Feig, M.; de Groot, B. L.; Grubmüller, H.; MacKerell, A. D. CHARMM36m: an improved force field for folded and intrinsically disordered proteins. *Nat. Methods* **2017**, *14* (1), 71−73.
(102) Jorgensen, W. L.; Chandrasekhar, J.; Madura, J. D.; Impey, R. W.; Klein, M. L. Comparison of simple potential functions for simulating liquid water. *J. Chem. Phys.* **1983**, *79* (2), 926−935.
(103) Durell, S. R.; Brooks, B. R.; Ben-Naim, A. Solvent-Induced Forces between Two Hydrophilic Groups. *J. Phys. Chem.* **1994**, *98* (8), 2198−2202.
(104) Brooks, B. R.; Brooks, C. L., III; Mackerell, A. D., Jr.; Nilsson, L.; Petrella, R. J.; Roux, B.; Won, Y.; Archontis, G.; Bartels, C.; Boresch, S.; et al. CHARMM: The biomolecular simulation program. *J. Comput. Chem.* **2009**, *30* (10), 1545−1614.
(105) Shaw, D. E.; Grossman, J. P.; Bank, J. A.; Batson, B.; Butts, J. A.; Chao, J. C.; Deneroff, M. M.; Dror, R. O.; Even, A.; Fenton, C. H.et al. Anton 2: Raising the Bar for Performance and Programmability in a Special-Purpose Molecular Dynamics Supercomputer. In *SC '14: Proceedings of the International Conference for High Performance Computing, Networking, Storage and Analysis*; IEEE: 2014, pp 41−53.
(106) Park, S.; Im, W.; Pastor, R. W. Developing initial conditions for simulations of asymmetric membranes: a practical recommendation. *Biophys. J.* **2021**, *120* (22), 5041−5059.
(107) Chow, K.-H.; Ferguson, D. M. Isothermal-isobaric molecular dynamics simulations with Monte Carlo volume sampling. *Comput. Phys. Commun.* **1995**, *91* (1), 283−289.
(108) Nosé, S. A molecular dynamics method for simulations in the canonical ensemble. *Mol. Phys.* **1984**, *52* (2), 255−268.
(109) Hoover, W. G. Canonical dynamics: Equilibrium phase-space distributions. *Phys. Rev. A* **1985**, *31* (3), 1695−1697.
(110) Martyna, G. J.; Klein, M. L.; Tuckerman, M. Nosé−Hoover chains: The canonical ensemble via continuous dynamics. *J. Chem. Phys.* **1992**, *97* (4), 2635−2643.
(111) Goodwin, D. G.; Moffat, H. K.; Schoegl, I.; Speth, R. L.; Weber, B. W. *Cantera: An Object-oriented Software Toolkit for Chemical Kinetics, Thermodynamics, and Transport Processes*, Zenodo: 2022.
(112) Miyamoto, S.; Kollman, P. A. Settle: An analytical version of the SHAKE and RATTLE algorithm for rigid water models. *J. Comput. Chem.* **1992**, *13* (8), 952−962.
(113) Eastman, P.; Pande, V. S. Constant Constraint Matrix Approximation: A Robust, Parallelizable Constraint Method for Molecular Simulations. *J. Chem. Theory Comput.* **2010**, *6* (2), 434−437.
(114) Darden, T.; York, D.; Pedersen, L. Particle mesh Ewald: An N·log(N) method for Ewald sums in large systems. *J. Chem. Phys.* **1993**, *98* (12), 10089−10092.
(115) Lippert, R. A.; Predescu, C.; Ierardi, D. J.; Mackenzie, K. M.; Eastwood, M. P.; Dror, R. O.; Shaw, D. E. Accurate and efficient integration for molecular dynamics simulations at constant temperature and pressure. *J. Chem. Phys.* **2013**, *139* (16), No. 164106.
(116) Humphrey, W.; Dalke, A.; Schulten, K. VMD: Visual molecular dynamics. *J. Mol. Graphics* **1996**, *14* (1), 33−38.
(117) Romo, T. D.; Grossfield, A. LOOS: An extensible platform for the structural analysis of simulations. In *2009 Annual International Conference of the IEEE Engineering in Medicine and Biology Society*; IEEE: 2009, pp 2332−2335.
(118) Roe, D. R.; Cheatham, T. E., III PTRAJ and CPPTRAJ: Software for Processing and Analysis of Molecular Dynamics Trajectory Data. *J. Chem. Theory Comput.* **2013**, *9* (7), 3084−3095.
(119) Szleifer, I.; Kramer, D.; Ben-Shaul, A.; Gelbart, W. M.; Safran, S. A. Molecular theory of curvature elasticity in surfactant films. *J. Chem. Phys.* **1990**, *92* (11), 6800−6817.
(120) Guixà-González, R.; Rodriguez-Espigares, I.; Ramírez-Anguita, J. M.; Carrió-Gaspar, P.; Martinez-Seara, H.; Giorgino, T.; Selent, J. MEMBPLUGIN: studying membrane complexity in VMD. *Bioinformatics* **2014**, *30* (10), 1478−1480.
(121) Huang, H. W. Action of antimicrobial peptides: Two-state model. *Biochemistry* **2000**, *39*, 8347−8352.
(122) Seelig, J.; Macdonald, P. M.; Scherer, P. G. Phospholipid head groups as sensors of electric charge in membranes. *Biochemistry* **1987**, *26* (24), 7535−41.
(123) Su, Y.; DeGrado, W. F.; Hong, M. Orientation, dynamics, and lipid interaction of an antimicrobial arylamide investigated by 19F and 31P solid-state NMR spectroscopy. *J. Am. Chem. Soc.* **2010**, *132* (26), 9197−205.
(124) Henzler-Wildman, K. A.; Lee, D. K.; Ramamoorthy, A. Mechanism of lipid bilayer disruption by the human antimicrobial peptide, LL-37. *Biochemistry* **2003**, *42*, 6545−6558.
(125) Bechinger, B.; Salnikov, E. S. The membrane interactions of antimicrobial peptides revealed by solid-state NMR spectroscopy. *Chem. Phys. Lipids* **2012**, *165* (3), 282−301.
(126) Ouellet, M.; Otis, F.; Voyer, N.; Auger, M. Biophysical studies of the interactions between 14-mer and 21-mer model amphipathic peptides and membranes: Insights on their modes of action. *Biochim Biophys Acta Biomembr* **2006**, *1758* (9), 1235−1244.
(127) Tremouilhac, P.; Strandberg, E.; Wadhwani, P.; Ulrich, A. S. Conditions affecting the re-alignment of the antimicrobial peptide PGLa in membranes as monitored by solid state 2H-NMR. *Biochimica et biophysica acta* **2006**, *1758* (9), 1330−42.
(128) Marcotte, I.; Wegener, K.; Lam, Y.; Chia, B.; de Planque, M.; Bowie, J.; Auger, M.; Separovic, F. Interaction of antimicrobial peptides from Australian amphibians with lipid membranes. *Chem. Phys. Lipids.* **2003**, *122*, 107−20.
(129) Wang, J.; Denny, J.; Tian, C.; Kim, S.; Mo, Y.; Kovacs, F.; Song, Z.; Nishimura, K.; Gan, Z.; Fu, R.; et al. Imaging membrane protein helical wheels. *J. Magn. Reson.* **2000**, *144* (1), 162−167.
(130) Marassi, F. M.; Opella, S. J. A solid-state NMR index of helical membrane protein structure and topology. *J. Magn. Reson.* **2000**, *144* (1), 150−155.
(131) De Angelis, A. A.; Grant, C. V.; Baxter, M. K.; McGavin, J. A.; Opella, S. J.; Cotten, M. L. Amphipathic Antimicrobial Piscidin in Magnetically Aligned Lipid Bilayers. *Biophys. J.* **2011**, *101* (5), 1086−1094.
(132) Fu, R.; Truong, M.; Saager, R. J.; Cotten, M.; Cross, T. A. High Resolution Heteronuclear Correlation Spectroscopy in Solid State NMR of Aligned Samples. *J. Magn. Reson.* **2007**, *188*, 41−48.
(133) Nevzorov, A. A.; Opella, S. J. Selective averaging for high-resolution solid-state NMR spectroscopy of aligned samples. *J. Magn. Reson.* **2007**, *185* (1), 59−70.
(134) Venable, R. M.; Brown, F. L. H.; Pastor, R. W. Mechanical properties of lipid bilayers from molecular dynamics simulation. *Chemistry and physics of lipids* **2015**, *192*, 60−74.
(135) Sodt, A. J.; Pastor, R. W. Molecular Modeling of Lipid Membrane Curvature Induction by a Peptide: More than Simply Shape. *Biophys. J.* **2014**, *106* (9), 1958−1969.
(136) Rice, A.; Haldar, S.; Wang, E.; Blank, P. S.; Akimov, S. A.; Galimzyanov, T. R.; Pastor, R. W.; Zimmerberg, J. Planar aggregation of the influenza viral fusion peptide alters membrane structure and hydration, promoting poration. *Nat. Commun.* **2022**, *13* (1), 7336.
(137) Ivanova, P. T.; Myers, D. S.; Milne, S. B.; McClaren, J. L.; Thomas, P. G.; Brown, H. A. Lipid composition of viral envelope of three strains of influenza virus - not all viruses are created equal. *ACS Infect. Dis.* **2015**, *1* (9), 435−442.
(138) Kawabata, K.; Sato, Y.; Kubo, T.; Tokumura, A.; Nishi, H.; Morimoto, K. Phospholipid analysis of two influenza A virus-infected cell lines differing in their viral replication kinetics. *Arch. Virol.* **2023**, *168* (5), 132.

https://doi.org/10.1021/acs.jpcb.4c05845
J. Phys. Chem. B 2025, 129, 210−227

(139) Koundouros, N.; Poulogiannis, G. Reprogramming of fatty acid metabolism in cancer. *Br. J. Cancer* **2020**, *122* (1), 4−22.
(140) Oludiran, A.; Courson, D. S.; Stuart, M. D.; Radwan, A. R.; Poutsma, J. C.; Cotten, M. L.; Purcell, E. B. How Oxygen Availability Affects the Antimicrobial Efficacy of Host Defense Peptides: Lessons Learned from Studying the Copper-Binding Peptides Piscidins 1 and 3. *Int. J. Mol. Sci.* **2019**, *20* (21), 5289.
(141) Holtrup, S.; Greger, M.; Mayer, B.; Specht, M.; Waidner, B. Insights Into the Helical Shape Complex of Helicobacter pylori. *Front Microbiol* **2022**, *13*, No. 929194.
(142) Chen, Z.; Rand, R. P. The influence of cholesterol on phospholipid membrane curvature and bending elasticity. *Biophys. J.* **1997**, *73* (1), 267−276.
(143) Teague, W. E., Jr.; Soubias, O.; Petrache, H.; Fuller, N.; Hines, K. G.; Rand, R. P.; Gawrisch, K. Elastic properties of polyunsaturated phosphatidylethanolamines influence rhodopsin function. *Faraday Discuss.* **2013**, *161*, 383−95. discussion 419−59
(144) Zhelev, D. V. Material property characteristics for lipid bilayers containing lysolipid. *Biophys. J.* **1998**, *75* (1), 321−30.
(145) Basañez, G.; Sharpe, J. C.; Galanis, J.; Brandt, T. B.; Hardwick, J. M.; Zimmerberg, J. Bax-type apoptotic proteins porate pure lipid bilayers through a mechanism sensitive to intrinsic monolayer curvature. *J. Biol. Chem.* **2002**, *277* (51), 49360−5.
(146) Woo, S. Y.; Lee, H. Effect of lipid shape on toroidal pore formation and peptide orientation in lipid bilayers. *Phys. Chem. Chem. Phys.* **2017**, *19* (32), 21340−21349.
(147) Wimley, W. C.; White, S. H. Experimentally determined hydrophobicity scale for proteins at membrane interfaces. *Nat. Struct. Biol.* **1996**, *3* (10), 842−848.
(148) Henzler-Wildman, K. A.; Martinez, G. V.; Brown, M. F.; Ramamoorthy, A. Perturbation of the hydrophobic core of lipid bilayers by the human antimicrobial peptide LL-37. *Biochemistry* **2004**, *43*, 8459−8469.
(149) Wimley, W. C. Describing the mechanism of antimicrobial peptide action with the interfacial activity model. *ACS Chem. Biol.* **2010**, *5* (10), 905−917.
(150) Blyth, G. A. D.; Connors, L.; Fodor, C.; Cobo, E. R. The Network of Colonic Host Defense Peptides as an Innate Immune Defense Against Enteropathogenic Bacteria. *Front. Immunol.* **2020**, *11*, 965.
(151) Baym, M.; Stone, L. K.; Kishony, R. Multidrug evolutionary strategies to reverse antibiotic resistance. *Science* **2016**, *351*, No. aad3292.
(152) Hanson, M. A.; Dostálová, A.; Ceroni, C.; Poidevin, M.; Kondo, S.; Lemaitre, B. Synergy and remarkable specificity of antimicrobial peptides in vivo using a systematic knockout approach. *eLife* **2019**, *8*, No. e44341.
(153) Hu, H.; Guo, N.; Chen, S.; Guo, X.; Liu, X.; Ye, S.; Chai, Q.; Wang, Y.; Liu, B.; He, Q. Antiviral activity of Piscidin 1 against pseudorabies virus both in vitro and in vivo. *Virol. J.* **2019**, *16* (1), 95.
(154) Lei, Z.; Liu, Q.; Zhu, Q.; Yang, B.; Khaliq, H.; Sun, A.; Qi, Y.; Moku, G. K.; Su, Y.; Wang, J.; et al. Comparative Pharmacokinetics and Preliminary Pharmacodynamics Evaluation of Piscidin 1 Against PRV and PEDV in Rats. *Front. Chem.* **2018**, *6*, 244.
(155) Chinchar, V. G.; Bryan, L.; Silphaduang, U.; Noga, E.; Wade, D.; Rollins-Smith, L. Inactivation of viruses infecting ectothermic animals by amphibian and piscine antimicrobial peptides. *Virology* **2004**, *323* (2), 268−275.
(156) Wang, G.; Watson, K. M.; Peterkofsky, A.; Buckheit, R. W., Jr Identification of novel human immunodeficiency virus type 1-inhibitory peptides based on the antimicrobial peptide database. *Antimicrob. Agents Chemother.* **2010**, *54* (3), 1343−1346.
(157) Wang, G. Database-guided discovery of potent peptides to combat HIV-1 or superbugs. *Pharmaceuticals* **2013**, *6* (6), 728−758.
(158) Bepler, T.; Barrera, M. D.; Rooney, M. T.; Xiong, Y.; Kuang, H.; Goodell, E.; Goodwin, M. J.; Harbron, E.; Fu, R.; Mihailescu, M.; et al. Antiviral activity of the host defense peptide piscidin 1: investigating a membrane-mediated mode of action. *Front. Chem.* **2024**, *12*, No. 1379192.
(159) Boto, A.; Pérez de la Lastra, J. M.; González, C. C. The Road from Host-Defense Peptides to a New Generation of Antimicrobial Drugs. *Molecules* **2018**, *23* (2), 311.
(160) Zambrowicz, A.; Timmer, M.; Polanowski, A.; Lubec, G.; Trziszka, T. Manufacturing of peptides exhibiting biological activity. *Amino Acids* **2013**, *44* (2), 315−20.
(161) Uhlig, T.; Kyprianou, T.; Martinelli, F. G.; Oppici, C. A.; Heiligers, D.; Hills, D.; Calvo, X. R.; Verhaert, P. The emergence of peptides in the pharmaceutical business: From exploration to exploitation. *EuPA Open Proteomics* **2014**, *4*, 58−69.
(162) Lin, H.-J.; Huang, T.-C.; Muthusamy, S.; Lee, J.-F.; Duann, Y.-F.; Lin, C.-H. Piscidin-1, an Antimicrobial Peptide from Fish (Hybrid Striped Bass Morone saxatilis x M. chrysops), Induces Apoptotic and Necrotic Activity in HT1080 Cells. *Zoolog. Sci.* **2012**, *29* (5), 327−332.
(163) Cheng, M. H.; Pan, C. Y.; Chen, N. F.; Yang, S. N.; Hsieh, S.; Wen, Z. H.; Chen, W. F.; Wang, J. W.; Lu, W. H.; Kuo, H. M. Piscidin-1 Induces Apoptosis via Mitochondrial Reactive Oxygen Species-Regulated Mitochondrial Dysfunction in Human Osteosarcoma Cells. *Sci. Rep.* **2020**, *10* (1), 5045.
(164) Wang, L.; Dong, C.; Li, X.; Han, W.; Su, X. Anticancer potential of bioactive peptides from animal sources (Review). *Oncol. Rep.* **2017**, *38* (2), 637−651.
(165) Gaspar, D.; Veiga, A. S.; Castanho, M. A. R. B. From antimicrobial to anticancer peptides. A review. *Front. Microbiol.* **2013**, *4*, 294.
(166) Gabernet, G.; Müller, A. T.; Hiss, J. A.; Schneider, G. Membranolytic anticancer peptides. *MedChemComm* **2016**, *7* (12), 2232−2245.
(167) Gabernet, G.; Gautschi, D.; Müller, A. T.; Neuhaus, C. S.; Armbrecht, L.; Dittrich, P. S.; Hiss, J. A.; Schneider, G. In silico design and optimization of selective membranolytic anticancer peptides. *Sci. Rep.* **2019**, *9* (1), 11282.
(168) Felício, M. R.; Silva, O. N.; Gonçalves, S.; Santos, N. C.; Franco, O. L. Peptides with Dual Antimicrobial and Anticancer Activities. *Front. Chem.* **2017**, *5*, 5.
(169) Sanderson, J. M. The association of lipids with amyloid fibrils. *J. Biol. Chem.* **2022**, *298* (8), No. 102108.

NOTE ADDED AFTER ASAP PUBLICATION

This paper was published December 16, 2024, with errors in the Supporting Information and several errors in the paper's text. The corrected version reposed December 23, 2024.

https://doi.org/10.1021/acs.jpcb.4c05845
J. Phys. Chem. B 2025, 129, 210−227